

<sub>1</sub> A novel inf–sup–based volumetric constraint ratio and  
<sub>2</sub> its implementation via mixed FE-meshfree formulation

<sub>3</sub> Junchao Wu<sup>a,\*</sup>, Yingjie Chu<sup>b</sup>, Yangtao Xu<sup>a</sup>

<sup>a</sup> Key Laboratory for Intelligent Infrastructure and Monitoring of Fujian Province, College  
of Civil Engineering, Huaqiao University , Xiamen, Fujian, 361021, China

<sup>b</sup> Fujian Key Laboratory of Digital Simulations for Coastal Civil Engineering, Department  
of Civil Engineering, Xiamen University , Xiamen, Fujian, 361005, China

---

<sub>4</sub> **Abstract**

Numerical formulations for incompressible materials often suffer from volumetric locking, which reduces the accuracy of displacement solutions and introduces oscillations in the pressure field. A well-chosen constraint ratio can mitigate this issue, but traditional approaches lack a theoretical foundation based on the inf–sup (or LBB) condition, which is essential for the stability of mixed formulations. This paper introduces a novel optimal constraint ratio derived from the inf–sup condition to address volumetric locking. The inf–sup test, a numerical tool for verifying the inf–sup condition, is reaffirmed to be equivalent to the inf–sup condition through a variational approach. By incorporating a complete polynomial space whose dimension matches the number of displacement degrees of freedom (DOFs), a new inf–sup value estimator is developed, explicitly considering the constraint ratio. For a given number of displacement DOFs, when the pressure DOFs of a numerical formulation remain below a stabilized number that falls into the optimal constraint ratio range, this numerical formulation actually satisfies the inf–sup condition. To implement the optimal constraint ratio, a mixed finite element and meshfree formulation is proposed, where displacements are discretized using traditional finite element approximations, and pressures are approximated via the reproducing kernel meshfree method. Leveraging the globally smooth reproducing kernel shape functions, the constraint ratio can be flexibly adjusted to meet the inf–sup condition without the limit of element. For computational efficiency and ease of implementation, pressure nodes are placed on selected displacement nodes to maintain the optimal constraint ratio. Inf–sup tests and a series of 2D and 3D incompressible elasticity examples validate the proposed constraint ratio, demonstrating its effectiveness in eliminating volumetric locking and enhancing the performance of mixed finite element and meshfree formulations.

<sub>5</sub> **Keywords:** Optimal constraint ratio, Inf–sup condition estimator, Volumetric  
<sub>6</sub> locking, Mixed formulation, Reproducing kernel meshfree approximation

---

---

\*Corresponding author  
Email address: jcwu@hqu.edu.cn (Junchao Wu)

7      **1. Introduction**

8      The volumetric constraint is a necessary condition in the numerical formulation  
 9      of incompressible materials like rubber and hydrogel. Proper imposition of  
 10     this constraint is crucial for obtaining better numerical solutions; insufficient or  
 11     excessive constraints will reduce the accuracy and stability of the solution [1].  
 12     The volumetric constraint ratio [2], denoted as  $r$ , is often used to measure the  
 13     level of constraint. It is defined as the total degrees of freedom (DOFs) of dis-  
 14     placement divided by the total DOFs of pressure. Ideally, the optimal constraint  
 15     ratio should be consistent with its governing partial differential equations. For  
 16     example, in the two-dimensional (2D) case, the optimal constraint ratio is 2,  
 17     since there are two governing equations for displacement and one for pressure.  
 18     When the constraint ratio is less than 2, the formulation suffers from volumetric  
 19     locking, while a constraint ratio greater than 2 can cause a coarse solution for  
 20     pressure. These observations have been summarized as follows[2]:

$$r = \frac{2n_u}{n_p}, \quad \begin{cases} r > 2 & \text{too few constraints} \\ r = 2 & \text{optimal} \\ r < 2 & \text{too many constraints} \\ r \leq 1 & \text{severe locking} \end{cases} \quad (1)$$

21     where  $n_u$  and  $n_p$  are the numbers of control nodes for displacement and pressure,  
 22     respectively. Classifying the locked status via the constraint ratio is straight-  
 23     forward but imprecise. For instance, the constraint ratio can remain 2 while  
 24     the pressure is discretized using continuous shape functions identical to the  
 25     displacement's approximation. However, volumetric locking still exists in this  
 26     formulation [2].

27     The inf-sup condition, also known as the Ladyzhenskay–Babuka–Brezzi  
 28     (LBB) condition [3, 4], is a more precise requirement for a locking-free for-  
 29     mulation. This condition is based on the mixed formulation framework, and  
 30     when the inf-sup condition is satisfied, both the accuracy and stability of the  
 31     mixed-formulation can be ensured. However, verifying the inf-sup condition is  
 32     non-trivial. An eigenvalue problem namely inf-sup test can be used to check  
 33     this condition numerically [5, 6, 7, 8]. Analytically, Brezzi and Fortin proposed  
 34     a two-level projection framework that always satisfies the inf-sup condition, al-  
 35     lowing it to be checked by identifying whether the formulation is included in  
 36     this framework. Both analytical and numerical methods to check the inf-sup  
 37     condition are complex, and the relationship between the constraint ratio and  
 38     the inf-sup condition remains unclear.

39     To address volumetric constraint issues, adjusting the constraint ratio to an  
 40     appropriate level is commonly used and easily implemented. In traditional finite  
 41     element methods (FEM), this adjustment is carried out based on elements since  
 42     the DOFs are embedded in each element. Conventional FEM often exhibits  
 43     an over-constrained status. Reducing the approximation order of pressure in  
 44     mixed formulation can alleviate the constraint burden, such as with the well-  
 45     known Q4P1 (4-node quadrilateral displacement element with 1-node piecewise

constant pressure element) and Q8P3. Globally, using continuous shape functions to link the local pressure DOFs in each element can also reduce the total number of pressure DOFs and increase the constraint ratio, such as with T6C3 (6-node triangular displacement element with 3-node continuous linear pressure element) and Q9C4 (Taylor–Hood element) [9]. These schemes belong to the mixed formulation framework and can also be implemented through a projection approach, where the pressure approximant is projected into a lower-dimensional space. Examples include selective integration methods [10, 11], B–bar or F–bar methods [12, 13, 14, 15], pressure projection methods [16, 17, 18, 19, 20], and enhanced strain method [21]. Meanwhile, conventional 3-node triangular elements arranged in a regular cross pattern can also reduce the dimension of the pressure space [22]. It should be noted that not all of these methods meet the inf–sup condition despite alleviating volumetric locking and producing a good displacement solution. Some methods, like Q4P1, show significant oscillation for the pressure solution, known as spurious pressure mode or checkerboard mode [22]. In such cases, additional stabilization approaches, such as variational multi-scale stabilization (VMS) [23, 24, 25, 26, 27], Galerkin/least-squares (GLS) [28], or Streamline upwind/Petrov–Galerkin formulation (SUPG) [29, 30] are required to eliminate the oscillations in pressure.

Another class of FEM methods adjusts the constraint ratio by increasing the displacement DOFs. For instance, based on 3-node triangular elements, Arnold et al. [31, 32] used a cubic bubble function in each element to increase the displacement DOFs, known as the MINI element. It has been shown that this method belongs to the VMS framework [33], and its fulfillment of the inf–sup condition can be analytically evidenced using the two-level projection framework [7]. The Crouzeix–Raviart element [34] transfers the DOFs from the triangular vertices to edges, increasing the constraint ratio since, for triangular topology, the number of edges is greater than that of vertices. More details about FEM technology for volumetric constraint issues can be found in Refs. [2, 4, 35].

In the past two decades, various novel approximations equipped with globally smooth shape functions, such as moving least-squares approximation [36], reproducing kernel approximation [37, 38], radial basis functions [39, 40], maximum-entropy approximation [41], and NURBS approximation [42, 43], have been proposed. In these approaches, the approximant pressure evaluated by the derivatives of globally continuous shape functions also maintains a constraint ratio of 2 in 2D incompressible elasticity problems. However, the corresponding results still show lower accuracy caused by locking [44, 45]. Widely-used locking-free technologies for FEM are introduced in these approaches to enhance their performance. For example, Moutsanidis et al. [46, 47] employed selective integration and B–bar, F–bar methods for reproducing kernel particle methods. Wang et al. [48] applied selective integration schemes with bubble-stabilized functions to node-based smoothed particle FEM. Elguedj et al. [49] proposed the B–bar and F–bar NURBS formulations for linear and nonlinear incompressible elasticity. Chen et al. [50] adopted the pressure projection approach for reproducing kernel formulations for nearly-incompressible problems, which was later extended

to Stokes flow formulations by Goh et al. [51]. Bombarde et al. [52] developed a block-wise NURBS formulation for shell structures, eliminating locking via pressure projection. Casquero and Golestanian [53] proposed a NURBS-based continuous-assumed-strain element to alleviate volumetric locking. Most of these approximations offer better flexibility for arranging DOFs since their shape function constructions are no longer element-dependent. Huerta et al.[54] proposed a reproducing kernel approximation with divergence-free basis functions to avoid volumetric strain entirely , although this approach is unsuitable for compressible cases. Wu et al. [55] added extra displacement DOFs in FEM elements to resolve the locking issue, constructing local shape functions using generalized meshfree interpolation to maintain consistency. Vu-Huu et al. [56] employed different-order polygonal finite element shape functions to approximate displacement and pressure, embedding a bubble function in each element for stabilization.

This work proposes a more precise optimal volumetric constraint ratio and implements a locking-free mixed FE-meshfree formulation with this optimal constraint ratio. Firstly, the inf-sup condition is derived in a new form, showing that the inf-sup value equals to the lowest non-zero eigenvalue of dilatation stiffness in the context of variational analysis. Subsequently, involving a complete polynomial space with dimensions identical to displacement DOFs, the number of non-zero eigenvalues can be analytically calculated, and a new estimator considering the constraint ratio is established. From this estimator, the optimal constraint ratio is defined with a stabilized number of pressure nodes. If the constraint ratio exceeds the locking ratio, the formulation will show severe locking. When the constraint ratio is lower than the optimal ratio, the formulation achieves satisfactory results, and the inf-sup condition is fulfilled. This estimator provides a strong link between the inf-sup value and the pressure DOFs, making it possible to justify the locking status by counting the pressure nodes. Furthermore, a mixed FE-meshfree formulation is proposed to verify the optimal constraint ratio. In this mixed formulation, the displacement is approximated by traditional finite element methods, and the pressure is discretized by reproducing kernel meshfree approximation. With the aid of global RK shape functions, the pressure's DOFs can be adjusted arbitrarily without considering approximation order and numerical integration issues to maintaining the constraint ratio as optimal.

The remainder of this paper is organized as follows: Section 2 reviews the mixed formulation framework for incompressible elasticity problems. In Section 3, a novel estimator of the inf-sup value is developed, from which the optimal constraint ratio is obtained. Section 4 introduces the mixed FE-meshfree formulation and its corresponding nodal distribution schemes. Section 5 verifies the proposed optimal constraint ratio using a set of benchmark incompressible elasticity examples, studying error convergence and stability property for the mixed FE-meshfree approximation. Finally, the conclusions are presented in Section 6.

<sup>136</sup> **2. Mixed-formulation**

<sup>137</sup> *2.1. Nearly-incompressible elasticity*

<sup>138</sup> Consider a body  $\Omega \in \mathbb{R}^{n_d}$  with boundary  $\Gamma$  in  $n_d$ -dimension, where  $\Gamma_t$  and  
<sup>139</sup>  $\Gamma_g$  denote its natural boundary and essential boundary, respectively, such that  
<sup>140</sup>  $\Gamma_t \cup \Gamma_g = \Gamma$ ,  $\Gamma_t \cap \Gamma_g = \emptyset$ . The corresponding governing equations for the mixed  
<sup>141</sup> formulation are given by:

$$\begin{cases} \nabla \cdot \boldsymbol{\sigma} + \mathbf{b} = \mathbf{0} & \text{in } \Omega \\ \frac{p}{\kappa} + \nabla \cdot \mathbf{u} = 0 & \text{in } \Omega \\ \boldsymbol{\sigma} \cdot \mathbf{n} = \mathbf{t} & \text{on } \Gamma_t \\ \mathbf{u} = \mathbf{g} & \text{on } \Gamma_g \end{cases} \quad (2)$$

<sup>142</sup> where  $\mathbf{b}$  denotes the prescribed body force in  $\Omega$ .  $\mathbf{t}, \mathbf{g}$  are prescribed traction and  
<sup>143</sup> displacement on natural and essential boundaries, respectively.  $\mathbf{u}$  and  $p$ , standing  
<sup>144</sup> for displacement and hydrostatic pressure, respectively, are the variables of  
<sup>145</sup> this problem.  $\nabla$  is the gradient tensor defined by  $\nabla = \frac{\partial}{\partial x_i} \mathbf{e}_i$ .  $\boldsymbol{\sigma}$  denotes the  
<sup>146</sup> stress tensor and has the following form:

$$\boldsymbol{\sigma}(\mathbf{u}, p) = p \mathbf{1} + 2\mu \nabla^d \mathbf{u} \quad (3)$$

<sup>147</sup> in which  $\mathbf{1} = \delta_{ij} \mathbf{e}_i \otimes \mathbf{e}_j$  is the second-order identity tensor.  $\nabla^d \mathbf{u}$  is the deviatoric  
<sup>148</sup> gradient of  $\mathbf{u}$  and can be evaluated by:

$$\nabla^d \mathbf{u} = \frac{1}{2} (\mathbf{u} \nabla + \nabla \mathbf{u}) - \left( \frac{1}{3} \nabla \cdot \mathbf{u} \right) \mathbf{1} \quad (4)$$

<sup>149</sup> and  $\kappa, \mu$  are the bulk modulus and shear modulus, respectively, and they can  
<sup>150</sup> be represented by Young's modulus  $E$  and Poisson's ratio  $\nu$ :

$$\kappa = \frac{E}{2(1-2\nu)}, \quad \mu = \frac{E}{3(1+\nu)} \quad (5)$$

<sup>151</sup> In accordance with the Galerkin formulation, the weak form can be given  
<sup>152</sup> by: Find  $\mathbf{u} \in V, p \in Q$ , such that

$$\begin{cases} a(\mathbf{v}, \mathbf{u}) + b(\mathbf{v}, p) = f(\mathbf{v}) & \forall \mathbf{v} \in V \\ b(\mathbf{u}, q) + c(q, p) = 0 & \forall q \in Q \end{cases} \quad (6)$$

<sup>153</sup> with the spaces  $V, Q$  defined by:

$$V = \{ \mathbf{v} \in H^1(\Omega)^2 \mid \mathbf{v} = \mathbf{g}, \text{ on } \Gamma_g \} \quad (7)$$

$$Q = \{ q \in L^2(\Omega) \mid \int_{\Omega} q \, d\Omega = 0 \} \quad (8)$$

154 where  $a : V \times V \rightarrow \mathbb{R}$ ,  $b : V \times Q \rightarrow \mathbb{R}$  and  $c : Q \times Q \rightarrow \mathbb{R}$  are bilinear forms,  
 155 and  $f : V \rightarrow \mathbb{R}$  is the linear form. In elasticity problems, they are given by:

$$a(\mathbf{v}, \mathbf{u}) = \int_{\Omega} \nabla^d \mathbf{v} : \nabla^d \mathbf{u} d\Omega \quad (9)$$

$$b(\mathbf{v}, q) = \int_{\Omega} \nabla \cdot \mathbf{v} q d\Omega \quad (10)$$

$$c(q, p) = - \int_{\Omega} \frac{1}{3\kappa} q p d\Omega \quad (11)$$

$$f(\mathbf{v}) = \int_{\Gamma_t} \mathbf{v} \cdot \mathbf{t} d\Gamma + \int_{\Omega} \mathbf{v} \cdot \mathbf{b} d\Omega \quad (12)$$

156 *2.2. Ritz–Galerkin problem and volumetric locking*

157 In the mixed-formulation framework, the displacement and pressure can be  
 158 discretized by different approximations. The approximant displacement  $\mathbf{u}_h$  and  
 159 approximant pressure  $p_h$  can be expressed by:

$$\mathbf{u}_h(\mathbf{x}) = \sum_{I=1}^{n_u} N_I(\mathbf{x}) \mathbf{u}_I, \quad p_h(\mathbf{x}) = \sum_{K=1}^{n_p} \Psi_K(\mathbf{x}) p_K \quad (13)$$

160 where  $N_I$  and  $\Psi_K$  are the shape functions for the displacement and pressure,  $\mathbf{u}_I$   
 161 and  $p_K$  are the corresponding coefficients. Leading these approximations into  
 162 the weak form of Eq. (6) yields the following Ritz–Galerkin problems: Find  
 163  $\mathbf{u}_h \in V_h$ ,  $p_h \in Q_h$ , such that

$$\begin{cases} a(\mathbf{v}_h, \mathbf{u}_h) + b(\mathbf{v}_h, p_h) = f(\mathbf{v}_h) & \forall \mathbf{v}_h \in V_h \\ b(\mathbf{u}_h, q_h) + c(q_h, p_h) = 0 & \forall q_h \in Q_h \end{cases} \quad (14)$$

164 where the spaces  $V_h \subseteq V$ ,  $Q_h \subseteq Q$  are defined by:

$$V_h = \{\mathbf{v}_h \in (\text{span}\{N_I\}_{I=1}^{n_u})^{n_d} \mid \mathbf{v}_h^h = \mathbf{g}, \text{ on } \Gamma_g\} \quad (15)$$

$$Q_h = \{q_h \in \text{span}\{\Psi_K\}_{K=1}^{n_p} \mid \int_{\Omega} q_h d\Omega = 0\} \quad (16)$$

165 For nearly incompressible material, the Poisson ratio approaches 0.5, and  
 166 the bulk modulus  $\kappa$  will tend to infinity based on Eq. (5). Then, the bilinear  
 167 form  $c$  in Eq. (11) tends to zero. And the weak form of Eq. (14) becomes an  
 168 enforcement of the volumetric strain  $\nabla \cdot \mathbf{u}_h$  to be zero using the Lagrangian  
 169 multiplier method, where  $p_h$  is the Lagrangian multiplier.

170 Furthermore, from the second line of Eq. (14), we have:

$$b(\mathbf{u}_h, q_h) + c(q_h, p_h) = (q_h, \nabla \cdot \mathbf{u}_h) - (q_h, \frac{1}{3\kappa} p_h) = 0, \quad \forall q_h \in Q_h \quad (17)$$

171 or

$$(q_h, 3\kappa \nabla \cdot \mathbf{u}_h - p_h) = 0, \quad \forall q_h \in Q_h \quad (18)$$

<sup>172</sup> where  $(\bullet, \bullet)$  is the inner product operator evaluated by:

$$(q, p) := \int_{\Omega} q p d\Omega \quad (19)$$

<sup>173</sup> Obviously, in Eq. (18),  $p_h$  is the orthogonal projection of  $3\kappa \nabla \cdot \mathbf{u}_h$  with respect  
<sup>174</sup> to the space  $Q_h$  [1], and, for further development, we use the nabla notation  
<sup>175</sup> with an upper tilde to denote the projection operator, i.e.,  $p_h = \tilde{\nabla} \cdot \mathbf{u}_h$ . In this  
<sup>176</sup> circumstance, the bilinear form  $b$  in the first line of Eq. (14) becomes:

$$\begin{aligned} b(\mathbf{v}_h, p_h) &= (\underbrace{\nabla \cdot \mathbf{v}_h - \tilde{\nabla} \cdot \mathbf{v}_h, p_h}_{0}) + (\tilde{\nabla} \cdot \mathbf{v}_h, \underbrace{p_h}_{3\kappa \tilde{\nabla} \cdot \mathbf{u}_h}) \\ &= (\tilde{\nabla} \cdot \mathbf{v}_h, 3\kappa \tilde{\nabla} \cdot \mathbf{u}_h) \\ &= \tilde{a}(\mathbf{v}_h, \mathbf{u}_h) \end{aligned} \quad (20)$$

<sup>177</sup> where the bilinear form  $\tilde{a} : V_h \times V_h \rightarrow \mathbb{R}$  is defined by:

$$\tilde{a}(\mathbf{v}_h, \mathbf{u}_h) = \int_{\Omega} 3\kappa \tilde{\nabla} \cdot \mathbf{v}_h \tilde{\nabla} \cdot \mathbf{u}_h d\Omega \quad (21)$$

<sup>178</sup> Accordingly, the problem of Eq. (14) becomes a one-variable form: Find  
<sup>179</sup>  $\mathbf{u}_h \in V_h$ , such that

$$a(\mathbf{v}_h, \mathbf{u}_h) + \tilde{a}(\mathbf{v}_h, \mathbf{u}_h) = f(\mathbf{v}_h), \quad \forall \mathbf{v}_h \in V_h \quad (22)$$

<sup>180</sup> As  $\kappa \rightarrow \infty$ , Eq. (22) can be regarded as an enforcement of volumetric strain  
<sup>181</sup> using the penalty method, where  $\tilde{a}$  is the penalty term. However, it should  
<sup>182</sup> be noted that, if the mixed-formulation wants to obtain a satisfactory result,  
<sup>183</sup> this orthogonal projection must be surjective [57]. In the case where it is not  
<sup>184</sup> surjective, for a given  $p_h \in Q_h$ , it may not be possible to find a  $\mathbf{u}_h \in V_h$  such that  
<sup>185</sup>  $p_h = 3\kappa \nabla \cdot \mathbf{u}_h$ . This will lead to a much smaller displacement than expected and  
<sup>186</sup> an oscillated pressure result. This phenomenon is called volumetric locking.

### <sup>187</sup> 3. Optimal volumetric constraint ratio

#### <sup>188</sup> 3.1. Inf-sup condition and its eigenvalue problem

<sup>189</sup> To ensure the surjectivity of orthogonal projection and satisfactory results,  
<sup>190</sup> the approximations of Eq.(7) should satisfy the inf-sup condition, also known  
<sup>191</sup> as the [Ladyzhenskaya–Babuška–Brezzi](#) condition [4]:

$$\inf_{q_h \in Q_h} \sup_{\mathbf{v}_h \in V_h} \frac{|b(q_h, \mathbf{v}_h)|}{\|q_h\|_Q \|\mathbf{v}_h\|_V} \geq \beta > 0 \quad (23)$$

<sup>192</sup> in which  $\beta$ , namely the inf-sup value, is a constant independent of the charac-  
<sup>193</sup> terized element size  $h$ . The norms  $\|\bullet\|_V$  and  $\|\bullet\|_Q$  can be flexibly defined

<sup>194</sup> by:

$$\|\mathbf{v}\|_V^2 := \int_{\Omega} \nabla^d \mathbf{v} : \nabla^d \mathbf{v} \, d\Omega \quad (24)$$

$$\|q\|_Q^2 := \int_{\Omega} \frac{1}{3\kappa} q^2 \, d\Omega \quad (25)$$

<sup>195</sup> To establish the relationship between the inf-sup condition and the con-  
<sup>196</sup> straint ratio, the inf-sup condition is firstly transformed by the following Lemma  
<sup>197</sup> 1:

<sup>198</sup> **Lemma 1.** Suppose  $\mathcal{P}_h : V_h \rightarrow Q_h$  is the orthogonal projection operator of the  
<sup>199</sup> divergence operator  $\mathcal{P} := 3\kappa \nabla \cdot$ , i.e.,  $\mathcal{P}_h := 3\kappa \nabla \cdot$  and satisfies Eq. (18). Then,  
<sup>200</sup> the inf-sup value can be estimated by:

$$\beta \leq \inf_{V'_h \subset V_h \setminus \ker \mathcal{P}_h} \sup_{\mathbf{v}_h \in V'_h} \frac{\|\mathcal{P}_h \mathbf{v}_h\|_Q}{\|\mathbf{v}_h\|_V} \quad (26)$$

<sup>201</sup> in which  $\ker \mathcal{P}_h \subset V_h$  is the kernel of  $\mathcal{P}_h$  defined by  $\ker \mathcal{P}_h := \{\mathbf{v}_h \in V_h \mid \mathcal{P}_h \mathbf{v}_h = 0\}$ .

<sup>203</sup> PROOF. First, define the image space of  $\mathcal{P}_h$  as  $\text{Im} \mathcal{P}_h := \{p_h \in Q_h \mid \exists \mathbf{v}_h \in V_h, p_h = \mathcal{P}_h \mathbf{v}_h\}$ . Since  $\mathcal{P}_h \subset Q_h$ , Eq. (23) can be rewritten as:

$$\begin{aligned} \beta &\leq \inf_{q_h \in Q_h} \sup_{\mathbf{v}_h \in V_h} \frac{|b(q_h, \mathbf{v}_h)|}{\|q_h\|_Q \|\mathbf{v}_h\|_V} = \inf_{q_h \in Q_h} \sup_{\mathbf{v}_h \in V_h} \frac{|(q_h, \frac{1}{3\kappa} \mathcal{P} \mathbf{v}_h)|}{\|q_h\|_Q \|\mathbf{v}_h\|_V} \\ &\leq \inf_{q_h \in \text{Im} \mathcal{P}_h} \sup_{\mathbf{v}_h \in V_h} \frac{|\frac{1}{3\kappa} (q_h, \mathcal{P}_h \mathbf{v}_h)|}{\|q_h\|_Q \|\mathbf{v}_h\|_V} \end{aligned} \quad (27)$$

<sup>205</sup> For a given  $q_h \in \text{Im} \mathcal{P}_h$ , since both  $g_b$  and  $\mathcal{P}_h \mathbf{v}_h$  belong to  $\text{Im} \mathcal{P}_h$ ,  $\text{Im} \mathcal{P}_h \subset Q_h$ ,  
<sup>206</sup> according to the Cauchy-Schwarz inequality, we have:

$$\left| \frac{1}{3\kappa} (q_h, \mathcal{P}_h \mathbf{v}_h) \right| \leq \|q_h\|_Q \|\mathcal{P}_h \mathbf{v}_h\|_Q \quad (28)$$

<sup>207</sup> where this equality holds if and only if  $q_h = \mathcal{P}_h \mathbf{v}_h$ , i.e.,

$$\left| \frac{1}{3\kappa} (q_h, \mathcal{P}_h \mathbf{v}_h) \right| = \|q_h\|_Q \|\mathcal{P}_h \mathbf{v}_h\|_Q, \quad \forall \mathbf{v}_h \in V'_h \quad (29)$$

<sup>208</sup> the space  $V'_h \subset V_h \setminus \ker \mathcal{P}_h$  defined by:

$$V'_h = \{\mathbf{v}_h \in V_h \mid \mathcal{P}_h \mathbf{v}_h = q_h\} \quad (30)$$

<sup>209</sup> And the following relationship can be evidenced:

$$\sup_{\mathbf{v}_h \in V_h} \frac{|\frac{1}{3\kappa} (q_h, \mathcal{P}_h \mathbf{v}_h)|}{\|q_h\|_Q \|\mathbf{v}_h\|_V} = \sup_{\mathbf{v}_h \in V'_h} \frac{\|\mathcal{P}_h \mathbf{v}_h\|_Q}{\|\mathbf{v}_h\|_V}, \quad \exists q_h \in \text{Im} \mathcal{P}_h \quad (31)$$

<sup>210</sup> Consequently, by combining Eqs. (27) and (31), Eq. (26) can be obtained.

211 **Remark 1.** With Lemma 1 and the norm definitions in Eqs. (24),(25), the  
212 square of the inf-sup value can further be bounded by:

$$\beta^2 \leq \inf_{V'_h \subset V_h \setminus \ker \mathcal{P}_h} \sup_{\mathbf{v}_h \in V'_h} \frac{\|\mathcal{P}_h \mathbf{v}_h\|_Q^2}{\|\mathbf{v}_h\|_V^2} = \inf_{V'_h \subset V_h \setminus \ker \mathcal{P}_h} \sup_{\mathbf{v}_h \in V'_h} \frac{\tilde{a}(\mathbf{v}_h, \mathbf{v}_h)}{a(\mathbf{v}_h, \mathbf{v}_h)} \quad (32)$$

213 The left-hand side of the above equation is consistent with the minimum-maximum  
214 principle [58] and again proves the equivalence with the traditional numerical  
215 inf-sup test [5]. Since that,  $\beta^2$  evaluates the non-zero general eigenvalue of  $\tilde{a}$   
216 and  $a$  in Eq. (22).

### 217 3.2. Inf-sup value estimator

218 Subsequently, the relationship between constraint ratio and the inf-sup con-  
219 dition is established by the following Theorem:

220 **Theorem 1.** Suppose that  $\underline{P}_{n_u}$  is a complete polynomial space with  $n_u$  dimen-  
221 sions, and  $V_{n_u}$  is the polynomial displacement space,  $V_{n_u} = P_{n_u}^{n_d}$ . The inf-sup  
222 value  $\beta$  can further be bounded by:

$$\beta \leq \beta_s + O(h) \quad (33)$$

223 with

$$\beta_s = \inf_{V' \subset V_{n_u} \setminus \ker \mathcal{P}_h \mathcal{I}_h} \sup_{\mathbf{v} \in V'} \frac{\|\mathcal{P} \mathbf{v}\|_Q}{\|\mathbf{v}\|_V} \quad (34)$$

224 where  $\mathcal{I}_h$  is the interpolation operator of the displacement approximation, and  
225 correspondingly,  $O(h)$  is the remainder related to  $h$ .

226 PROOF. As the dimensions of  $V_h$  and  $V_{n_u}$  are identical,  $\dim V_{n_u} = \dim V_h =$   
227  $n_d \times n_u$ . There exists a unique  $\mathbf{v} \in V_{n_u}$  satisfying  $\mathbf{v}_h = \mathcal{I}_h \mathbf{v}$ . And the right side  
228 of Eq. (26) becomes:

$$\inf_{V'_h \subset V_h \setminus \ker \mathcal{P}_h} \sup_{\mathbf{v}_h \in V'_h} \frac{\|\mathcal{P}_h \mathbf{v}_h\|_Q}{\|\mathbf{v}_h\|_V} = \inf_{V' \subset V_{n_u} \setminus \ker \mathcal{P}_h \mathcal{I}_h} \sup_{\mathbf{v} \in V'} \frac{\|\mathcal{P}_h \mathcal{I}_h \mathbf{v}\|_Q}{\|\mathcal{I}_h \mathbf{v}\|_V} \quad (35)$$

229 According to the triangular inequality, Cauchy-Schwarz inequality, and the  
230 relationship of Eqs. (18), we have:

$$\begin{aligned} \|\mathcal{P}_h \mathcal{I}_h \mathbf{v}\|_Q &= \sup_{q_h \in Q_h} \frac{|\frac{1}{3\kappa}(q_h, \mathcal{P}_h \mathcal{I}_h \mathbf{v})|}{\|q_h\|_Q} = \sup_{q_h \in Q_h} \frac{|\frac{1}{3\kappa}(q_h, \mathcal{P} \mathcal{I}_h \mathbf{v})|}{\|q_h\|_Q} \\ &\leq \sup_{q_h \in Q_h} \frac{|\frac{1}{3\kappa}(q_h, \mathcal{P} \mathbf{v})| + |\frac{1}{3\kappa}(q_h, \mathcal{P} \mathbf{v} - \mathcal{P} \mathcal{I}_h \mathbf{v})|}{\|q_h\|_Q} \\ &\leq \|\mathcal{P} \mathbf{v}\|_Q + \|\mathcal{P}(\mathbf{v} - \mathcal{I}_h \mathbf{v})\|_Q \end{aligned} \quad (36)$$

231 Obviously, the second term on the right side of Eq. (36) is the interpolation  
232 error, and can be evaluated by [59]:

$$\|\mathcal{P}(\mathbf{v} - \mathcal{I}_h \mathbf{v})\|_Q \leq Ch^k |\mathbf{v}|_{H_k} \quad (37)$$

233 where, for a sufficiently smooth  $\mathbf{v} \in V$ ,  $k$  equals to the interpolation order of  
 234  $\mathcal{I}_h$ .

235 Further leading the relation  $\|\mathcal{I}_h \mathbf{v}\|_V \geq C|\mathbf{v}|_{H_k}$  obtained from the closed  
 236 graph theorem [33] and considering Eqs. (36)-(37), the right-hand side of Eq.  
 237 (35) can be represented as:

$$\inf_{V' \subset V_{n_u} \setminus \ker \mathcal{P}_h \mathcal{I}_h} \sup_{\mathbf{v} \in V'} \frac{\|\mathcal{P}_h \mathcal{I}_h \mathbf{v}\|_Q}{\|\mathcal{I}_h \mathbf{v}\|_V} \leq \inf_{V' \subset V_{n_u} \setminus \ker \mathcal{P}_h \mathcal{I}_h} \sup_{\mathbf{v} \in V'} \frac{\|\mathcal{P} \mathbf{v}\|_Q}{\|\mathbf{v}\|_V} + O(h) \quad (38)$$

238 Substituting Eqs. (35),(38) into (26) finally proves Eqs. (33), (34).

239 As we can see in Eqs. (33) and (34),  $\beta_s \geq 0$ , the condition that  $\beta_s$  being  
 240 equal to 0 or not determines whether the formulation can satisfy the inf-sup  
 241 condition. If  $\beta_s > 0$ , as the mesh refines, the second term on the right-hand  
 242 side of Eq. (33) will sharply reduce and can be ignored. In contrast, if  $\beta_s = 0$ ,  
 243 the second term will dominate, and the evaluation of  $\beta$  will be dependent to  $h$ .  
 244 Therefore, the inf-sup condition is violated and numerical instability arises.

### 245 3.3. Polynomial-wise constraint counting

246 From the above subsection, we can know that whether  $\beta_s$  is zero or not  
 247 determines whether the mixed-formulation can fulfill the inf-sup condition. Ac-  
 248 cording to the expression of  $\beta_s$  in Eq. (34), as  $\beta_s = 0$ , the variable  $\mathbf{v}$  should  
 249 belong to  $\ker \mathcal{P}$ , so the dimensions of the subspace in which  $\beta_s \neq 0$ , namely  $n_s$ ,  
 250 can be evaluated by:

$$n_s = \dim(V_{n_u} \setminus \ker \mathcal{P}) \quad (39)$$

251 To further construct the relationship between the inf-sup value estimator in  
 252 Eq. (33) and the constraint ratio  $r = \frac{n_d \times n_u}{n_p}$ , we should find the displacement  
 253 and pressure DOFs in Eq. (33). With the definition of  $V_{n_u}$ , the number of  
 254 displacement DOFs is easy to be evaluated by:

$$n_d \times n_u = \dim V_{n_u} \quad (40)$$

255 With well-posed nodal distributions of displacement and pressure, the number  
 256 of pressure DOFs has the following relationship:

$$n_p = \dim Q_h = \dim(\text{Im} \mathcal{P}_h) = \dim(V_{n_u} \setminus \ker \mathcal{P}_h \mathcal{I}_h) \quad (41)$$

257 Figure 1 illustrates how the relationship between  $n_s$ ,  $n_p$ , and  $n_u$  influences  
 258 the fulfillment of the inf-sup condition:

- 259 • As  $n_p > n_s$ , there must exist a subspace in space  $V_{n_u} \setminus \ker \mathcal{P}_h \mathcal{I}_h$  belonging  
 260 to  $\ker \mathcal{P}$ , resulting in  $\beta_s = 0$ , i.e.,  $V_{n_u} \setminus \ker \mathcal{P}_h \mathcal{I}_h \cap \ker \mathcal{P} \neq \emptyset$ . At this cir-  
 261 cumstance, the inf-sup condition cannot be satisfied, and the formulation  
 262 will suffer from volumetric locking.
- 263 • As  $n_p \leq n_s$ , for well-posed nodal distributions, the space  $V_{n_u} \setminus \ker \mathcal{P}_h \mathcal{I}_h$   
 264 may be a subset of  $V_{n_u} \setminus \ker \mathcal{P}$ . Then,  $\beta_s$  will remain nonzero, and the  
 265 formulation will be locking-free.

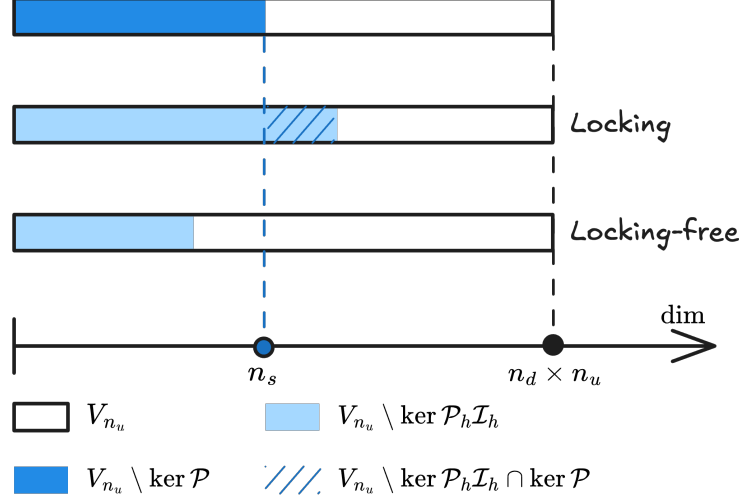


Figure 1: Illustration of estimator

266       Summarily, the formulation can satisfy the inf-sup condition and alleviate  
 267       volumetric locking if at least the number of pressure nodes  $n_p$  is less than  $n_s$ ,  
 268       so we name  $n_s$  as the stabilized number of pressure nodes. At this moment,  
 269       the volumetric constraint ratio should meet the following relation to ensure the  
 270       inf-sup condition:

$$r_{opt} \geq \frac{n_d \times n_u}{n_s} \quad (42)$$

271       **Remark 2.** Some uniform elements with special arrangements, like the union-  
 272       jack element arrangement for 3-node triangular elements, can pass the inf-sup  
 273       test [6], but their pressure DOFs number is greater than  $n_s$ . This is because the  
 274       union-jack arrangement leads to a lower nonzero eigenvalue number of  $\tilde{\alpha}$  and  $\alpha$   
 275       in Eq. (22), and the corresponding nonzero eigenvalue number is less than or  
 276       equal to the stabilized number  $n_s$ , satisfying Eq. (42). The similar cases about  
 277       this special element arrangement are too few, so it is more straightforward to  
 278       use the number of pressure nodes  $n_p$  to measure  $\dim(V_{n_u} \setminus \ker \mathcal{P}_h \mathcal{I}_h)$ .

279       **Remark 3.** It is obvious that the traditional optimal constraint ratio cannot  
 280       fulfill this condition. However, not all formulations satisfying this condition can  
 281       totally avoid volumetric locking. This is because  $n_p \leq n_s$  is not equivalent to  
 282        $V_{n_u} \setminus \ker \mathcal{P}_h \mathcal{I}_h \subset V_{n_u} \setminus \ker \mathcal{P}$ . Fortunately, well-posed nodal distributions of  
 283       displacement and pressure can ensure this, which will be evidenced by numerical  
 284       examples in the subsequent sections.

### 285       3.4. Optimal volumetric constraint ratio

286       The fulfillment of the inf-sup condition should require the number of pres-  
 287       sure nodes  $n_p$  to be lower than the stabilized number  $n_s$ , and now, we will  
 288       demonstrate how to determine  $n_s$  for a specific number of displacement DOFs.

<sup>289</sup> In the 2D case, for instance, we first consider the linear polynomial displacement  
<sup>290</sup> space  $V_3$  that is given by:

$$V_3 = \text{span} \left\{ \begin{pmatrix} 1 \\ 0 \end{pmatrix}, \begin{pmatrix} 0 \\ 1 \end{pmatrix}, \begin{pmatrix} x \\ 0 \end{pmatrix}, \begin{pmatrix} 0 \\ x \end{pmatrix}, \begin{pmatrix} y \\ 0 \end{pmatrix}, \begin{pmatrix} 0 \\ y \end{pmatrix} \right\} \quad (43)$$

<sup>291</sup> or rearranged as follows,

$$V_3 = \text{span} \left\{ \underbrace{\begin{pmatrix} 1 \\ 0 \end{pmatrix}, \begin{pmatrix} 0 \\ 1 \end{pmatrix}, \begin{pmatrix} y \\ 0 \end{pmatrix}, \begin{pmatrix} 0 \\ x \end{pmatrix}, \begin{pmatrix} x \\ -y \end{pmatrix}}_{\ker \mathcal{P}}, \underbrace{\begin{pmatrix} x \\ y \end{pmatrix}}_{V_3 \setminus \ker \mathcal{P}} \right\} \quad (44)$$

<sup>292</sup> It can be counted that, for  $n_u = 3$ ,  $n_s = 1$ . Following the path, the displacement  
<sup>293</sup> space with a quadratic polynomial base, namely  $V_6$ , can be stated as:

$$V_6 = \text{span} \left\{ \underbrace{\begin{pmatrix} 1 \\ 0 \end{pmatrix}, \begin{pmatrix} 0 \\ 1 \end{pmatrix}, \begin{pmatrix} y \\ 0 \end{pmatrix}, \begin{pmatrix} 0 \\ x \end{pmatrix}, \begin{pmatrix} x \\ -y \end{pmatrix}, \begin{pmatrix} x^2 \\ -2xy \end{pmatrix}, \begin{pmatrix} y^2 \\ 0 \end{pmatrix}, \begin{pmatrix} 0 \\ x^2 \end{pmatrix}, \begin{pmatrix} -2xy \\ y^2 \end{pmatrix}}_{\ker \mathcal{P}}, \underbrace{\begin{pmatrix} x \\ y \end{pmatrix}, \begin{pmatrix} x^2 \\ 2xy \end{pmatrix}, \begin{pmatrix} 2xy \\ y^2 \end{pmatrix}}_{V_6 \setminus \ker \mathcal{P}} \right\} \quad (45)$$

<sup>294</sup> In this circumstance,  $n_s = 3$ . As the order of the polynomial space increases,  
<sup>295</sup> the optimal numbers of constraint DOFs for each order of the polynomial space  
<sup>296</sup> are listed in Table. 1, in which  $n$  denotes the order of space  $P_{n_u}$ . For the  
<sup>297</sup> flexibility of usage, the relation between  $n_u$  and  $n_s$  is summarized as follows:

$$n_s = \frac{n(n+1)}{2}, \quad n = \left\lfloor \frac{\sqrt{1+8n_u}-3}{2} \right\rfloor \quad (46)$$

<sup>298</sup> where  $\lfloor \bullet \rfloor$  denotes the floor function.

Table 1: Relationship between the number of displacement nodes  $n_u$  and stabilized number of pressure nodes  $n_s$

$n$	2D		3D	
	$n_u$	$n_s$	$n_u$	$n_s$
1	3	1	4	1
2	6	3	10	4
3	10	6	20	10
4	15	10	35	20
$\vdots$	$\vdots$	$\vdots$	$\vdots$	$\vdots$

<sup>299</sup> For the 3D case, following the path in 2D, the linear polynomial space  $V_4$  is

<sup>300</sup> considered herein, and the arranged space of  $V_4$  is listed as follows:

$$V_4 = \text{span} \left\{ \underbrace{\begin{pmatrix} 1 \\ 0 \\ 0 \\ 0 \end{pmatrix}, \begin{pmatrix} 0 \\ 1 \\ 0 \\ 0 \end{pmatrix}, \begin{pmatrix} 0 \\ 0 \\ 1 \\ 1 \end{pmatrix}}_{\ker \mathcal{P}}, \underbrace{\begin{pmatrix} 0 \\ x \\ 0 \\ 0 \end{pmatrix}, \begin{pmatrix} 0 \\ 0 \\ x \\ 0 \end{pmatrix}, \begin{pmatrix} 0 \\ 0 \\ 0 \\ x \end{pmatrix}}_{\ker \mathcal{P}}, \underbrace{\begin{pmatrix} y \\ 0 \\ 0 \\ 0 \end{pmatrix}, \begin{pmatrix} z \\ 0 \\ 0 \\ 0 \end{pmatrix}, \begin{pmatrix} 0 \\ z \\ 0 \\ 0 \end{pmatrix}}_{V_{n_u} \setminus \ker \mathcal{P}}, \begin{pmatrix} x \\ y \\ z \\ 0 \end{pmatrix}, \begin{pmatrix} x \\ y \\ 0 \\ z \end{pmatrix} \right\} \quad (47)$$

<sup>301</sup> For brevity, the stabilized numbers for higher-order polynomial displacement  
<sup>302</sup> spaces are directly listed in Table. 1, and it can be summarized that, for a given  
<sup>303</sup> number of displacement DOFs, the stabilized number for pressure DOFs can be  
<sup>304</sup> calculated as follows:

$$n_s = \frac{n(n+1)(n+2)}{6} \quad (48)$$

$$n = \left[ \left( 3n_u + \frac{1}{3} \sqrt{81n_u^2 - \frac{1}{3}} \right)^{\frac{1}{3}} + \frac{1}{3 \left( 3n_u + \frac{1}{3} \sqrt{81n_u^2 - \frac{1}{3}} \right)^{\frac{1}{3}}} - 2 \right] \quad (49)$$

#### <sup>305</sup> 4. Mixed FE–meshfree formulation with optimal constraint ratio

<sup>306</sup> In the proposed mixed–formulation, the displacement is approximated using  
<sup>307</sup> 3-node (Tri3), 6-node (Tri6) triangular elements and 4-node (Quad4), 8-node  
<sup>308</sup> (Quad8) quadrilateral elements in 2D, 4-node (Tet4) tetrahedral element and  
<sup>309</sup> 8-node (Hex8) hexahedral element in 3D [2]. In order to flexibly adjust to  
<sup>310</sup> let the DOFs of pressure meet the optimal constraint, the reproducing kernel  
<sup>311</sup> meshfree approximation is involved to approximate pressure.

##### <sup>312</sup> 4.1. Reproducing kernel meshfree approximation

<sup>313</sup> In accordance with the reproducing kernel approximation, the entire domain  
<sup>314</sup>  $\Omega$ , as shown in Figure 2, is discretized by  $n_p$  meshfree nodes,  $\{\mathbf{x}_I\}_{I=1}^{n_p}$ . The  
<sup>315</sup> approximated pressure, namely  $p_h$ , can be expressed by the shape function  $\Psi_I$   
<sup>316</sup> and nodal coefficient  $p_I$ , yields:

$$p_h(\mathbf{x}) = \sum_{I=1}^{n_p} \Psi_I(\mathbf{x}) p_I \quad (50)$$

<sup>317</sup> where, in the reproducing kernel approximation framework, the shape function  
<sup>318</sup>  $\Psi_I$  is given by:

$$\Psi_I(\mathbf{x}) = \mathbf{c}(\mathbf{x}_I - \mathbf{x}) \mathbf{p}(\mathbf{x}_I - \mathbf{x}) \phi(\mathbf{x}_I - \mathbf{x}) \quad (51)$$

<sup>319</sup> in which  $\mathbf{p}$  is the basis vector, for instance in the context of the 3D quadratic  
<sup>320</sup> case, the basis vector takes the following form:

$$\mathbf{p}(\mathbf{x}) = \{1, x, y, z, x^2, y^2, z^2, xy, xz, yz\}^T \quad (52)$$

<sup>321</sup> and  $\phi$  stands for the kernel function. In this work, the traditional Cubic B-spline  
<sup>322</sup> function with square or cube support is used as the kernel function:

$$\phi(\mathbf{x}_I - \mathbf{x}) = \phi(s_x)\phi(s_y)\phi(s_z), \quad s_i = \frac{\|\mathbf{x}_I - \mathbf{x}\|}{\bar{s}_{iI}} \quad (53)$$

<sup>323</sup> with

$$\phi(s) = \frac{1}{3!} \begin{cases} (2-2s)^3 - 4(1-2s)^3 & s \leq \frac{1}{2} \\ (2-2s)^3 & \frac{1}{2} < s < 1 \\ 0 & s > 1 \end{cases} \quad (54)$$

<sup>324</sup> where  $\bar{s}_{iI}$ 's are the support size towards the  $i$ -direction for the shape function  
<sup>325</sup>  $\Psi_I$ . The correction function  $\mathbf{c}$  can be determined by the following so-called  
<sup>326</sup> consistency condition:

$$\sum_{I=1}^{n_p} \Psi_I(\mathbf{x}) \mathbf{p}(\mathbf{x}_I) = \mathbf{p}(\mathbf{x}) \quad (55)$$

<sup>327</sup> or equivalent shifted form:

$$\sum_{I=1}^{n_p} \Psi_I(\mathbf{x}) \mathbf{p}(\mathbf{x}_I - \mathbf{x}) = \mathbf{p}(\mathbf{0}) \quad (56)$$

<sup>328</sup> The consistency condition ensures that the reproducing kernel shape functions  
<sup>329</sup> are able to reproduce the polynomial space spanned by the basis function  $\mathbf{p}$ ,  
<sup>330</sup> which is a fundamental requirement for the accuracy of the Galerkin method.  
<sup>331</sup> Herein, the order of the basis function  $\mathbf{p}$  is chosen to be the same as the order  
<sup>332</sup> of the displacement approximation.

<sup>333</sup> Further, substituting Eq. 51 into Eq. (56) leads to:

$$\mathbf{c}(\mathbf{x}_I - \mathbf{x}) = \mathbf{A}^{-1}(\mathbf{x}_I - \mathbf{x}) \mathbf{p}(\mathbf{0}) \quad (57)$$

<sup>334</sup> in which  $\mathbf{A}$  is namely the moment matrix evaluated by:

$$\mathbf{A}(\mathbf{x}_I - \mathbf{x}) = \sum_{I=1}^{n_p} \mathbf{p}(\mathbf{x}_I - \mathbf{x}) \mathbf{p}^T(\mathbf{x}_I - \mathbf{x}) \phi(\mathbf{x}_I - \mathbf{x}) \quad (58)$$

<sup>335</sup> Taking Eq. (57) back to Eq. (51), the final form of the reproducing kernel shape  
<sup>336</sup> function can be obtained as:

$$\Psi_I(\mathbf{x}) = \mathbf{p}^T(\mathbf{0}) \mathbf{A}^{-1}(\mathbf{x}_I - \mathbf{x}) \phi(\mathbf{x}_I - \mathbf{x}) \quad (59)$$

<sup>337</sup> As shown in Figure 2, reproducing kernel meshfree shape functions are  
<sup>338</sup> globally smooth across the entire domain, using them to discretize the pres-  
<sup>339</sup> sure field allows the constraint ratio to be adjusted arbitrarily, without being  
<sup>340</sup> limited by element topology. Meshfree shape functions generally lack the

341 Kronecker delta property, which prevents the direct imposition of essential  
 342 boundary conditions. Fortunately, the mixed formulation shown in Eq. 14 only  
 343 concerns the displacement essential boundary condition, and this condition can  
 344 be easily imposed by the standard methods, such as the penalty method that  
 345 used in this work.

346 Moreover, when combined with finite element approximations in Eq. 14,  
 347 numerical integration can be conveniently performed within each finite ele-  
 348 ment ( $\Omega_C$ 's). The numerical integration issue caused by the loss of variational  
 349 consistency between meshfree shape functions and their derivatives [60] would  
 350 not appear in the mixed formulation of Eq. 14, this is due to the fact that Eq.  
 351 14 solely depends on the meshfree shape functions themselves. Therefore, the  
 352 proposed method employs standard lower-order Gaussian quadrature rules, as  
 353 commonly used in traditional finite element methods, while still maintaining its  
 354 accuracy.

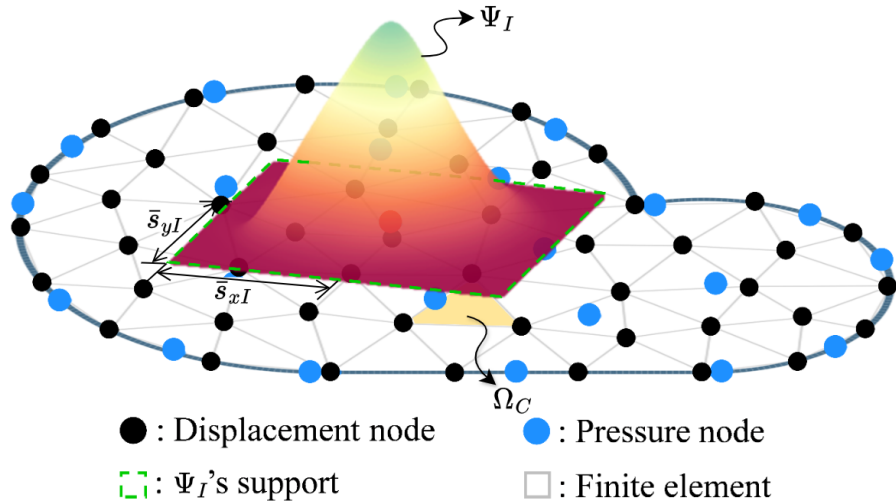


Figure 2: Illustration for reproducing kernel meshfree approximation

#### 355 4.2. Pressure node distributions with optimal constraint ratio

356 In this subsection, 2D and 3D inf-sup tests [6], as defined in Eq. 32, are con-  
 357 ducted using the mixed FE-meshfree formulations to validate the proposed inf-  
 358 sup value estimator. The 2D test considers the square domain  $\Omega = (0, 1) \times (0, 1)$ ,  
 359 where the displacement is discretized by Tri3 and Quad4 with  $4 \times 4$ ,  $8 \times 8$ ,  $16 \times 16$   
 360 and  $32 \times 32$  elements, Tri6 and Quad8 with  $2 \times 2$ ,  $4 \times 4$ ,  $8 \times 8$  and  $16 \times 16$  elements,  
 361 respectively. The 3D test employs a cube domain  $\Omega = (0, 1) \times (0, 1) \times (0, 1)$   
 362 with  $4 \times 4$ ,  $8 \times 8$  and  $16 \times 16$  elements for the Tet4 and Hex8. For pressure  
 363 discretization, linear meshfree approximation with a normalized support size  
 364 of 1.5 is employed for Tri3, Quad4, Tet4 and Hex8. For Tri6 and Quad8,

365 a quadratic meshfree approximation with a normalized support size of 2.5 is  
 366 utilized. In order to avoid the influence of interpolation error, uniform nodal  
 367 distributions are used for pressure discretizations, for example in Figure 3, which  
 368 displays  $4 \times 4$  Quad4 elements with  $4 \times 3$  uniformly distributed pressure nodes.

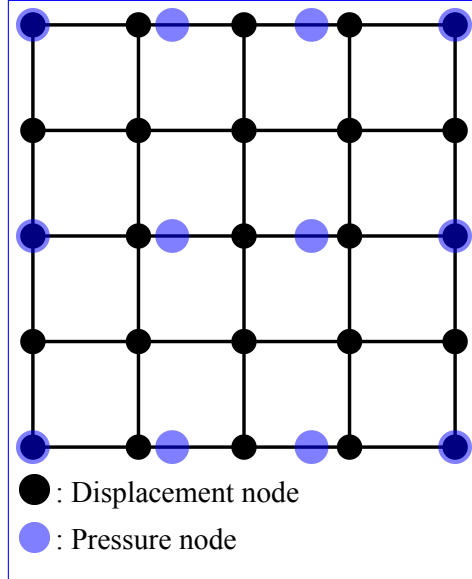


Figure 3: Illustration of uniform nodal distribution for inf-sup test with  $n_u = 5 \times 5$ ,  
 $n_p = 4 \times 3$

369 Figures 4–9 show the corresponding results, in which the red line stands for  
 370 the value of  $\beta$  with respect to the number of pressure nodes  $n_p$ , and the vertical  
 371 dashed line denotes the stabilized number  $n_s$ . The deeper color of the lines  
 372 means mesh refinement. The results show that, no matter linear or quadratic  
 373 elements, as  $n_p$  increases over  $n_s$ , the value of  $\beta$  sharply decreases, and then  
 374 the inf-sup condition cannot be maintained. This result is consistent with the  
 375 discussion in Section 3, and again verifies the effect of the proposed estimator.

376 Moreover, the mixed formulation's results with the traditional optimal con-  
 377 straint ratio  $r = n_d$  are listed in these figures as well, and  $\beta$  in this circumstance  
 378 is already much smaller than those in the optimal range. Considering the re-  
 379 sults shown above, the easy programming and efficiency, the pressure nodes  
 380 are chosen among the displacement nodes. The optimal schemes for linear and  
 381 quadratic, 2D and 3D element discretizations, namely with  $r = r_{opt}$ , are shown  
 382 in Figure 10, where every other displacement node is selected as the pressure  
 383 node. For practical implementations of linear cases, the pressure nodes are  
 384 initially generated using traditional approaches, such as Delaunay triangulation.  
 385 Subsequently, the displacement nodes are then obtained through a standard  
 386 mesh refinement process to the pressure nodes. For quadratic approximations in  
 387 Tri6 and Quad8 elements, the element vertices are chosen as pressure nodes after

388 displacement element generation. Consequently, all constraint ratios evaluated  
 389 using the discretizations in Figure 10 fall within the optimal range. The corre-  
 390 sponding inf-sup test results for these schemes are also marked in inf-sup test  
 391 figure and show that, with mesh refinement, their  $\beta$ 's are always maintained at  
 392 a non-negligible level.

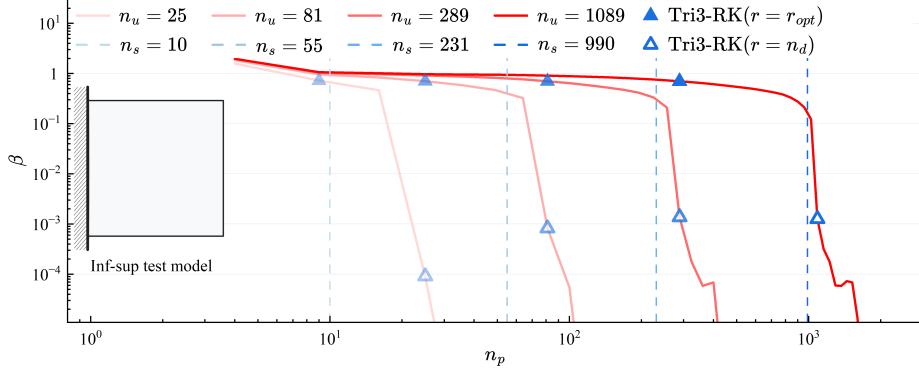


Figure 4: Inf-sup test for Tri3-RK

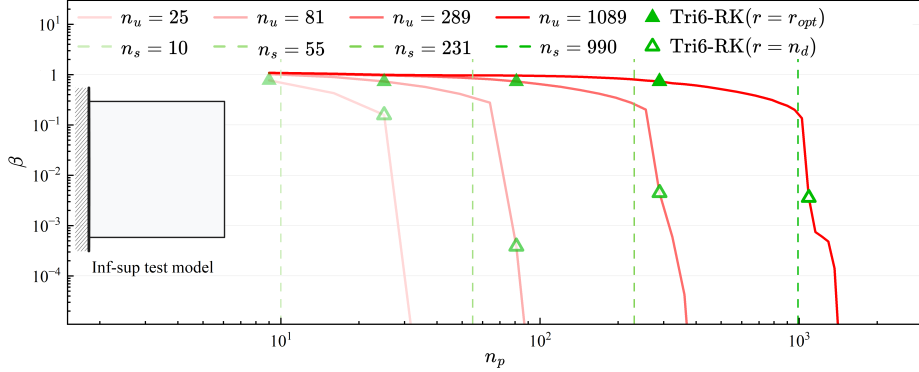


Figure 5: Inf-sup test for Tri6-RK

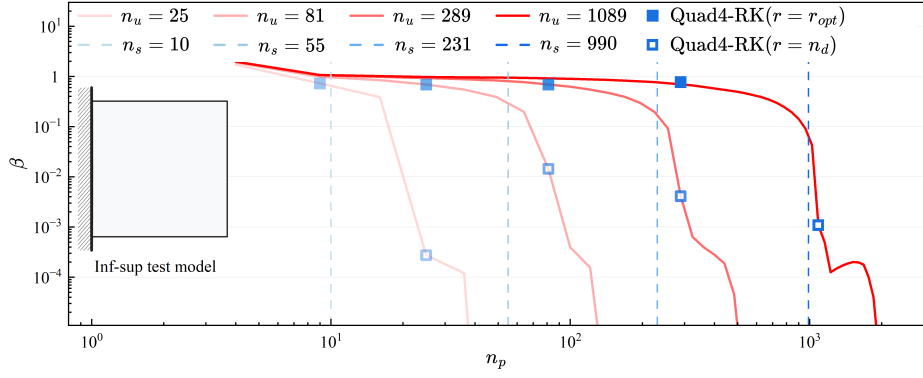


Figure 6: Inf-sup test for Quad4-RK

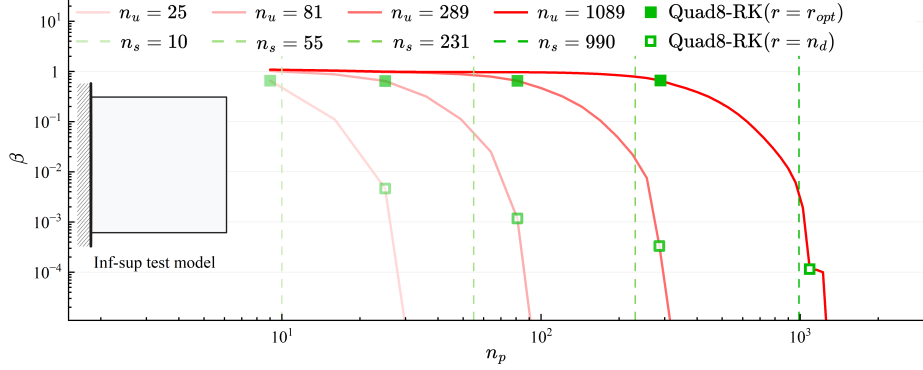


Figure 7: Inf-sup test for Quad8-RK

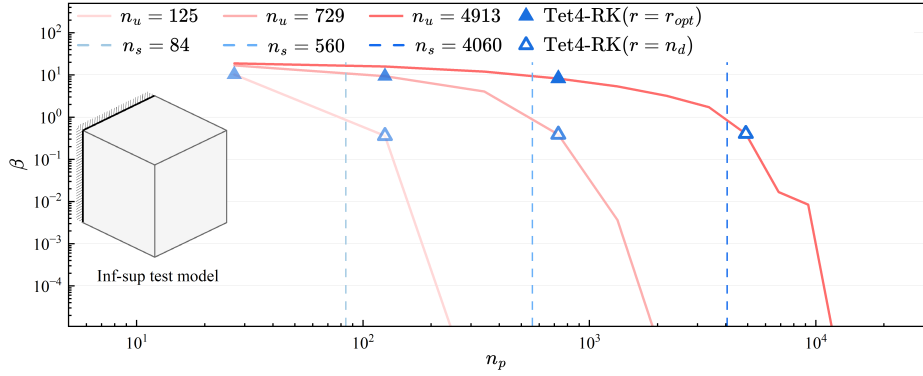


Figure 8: Inf-sup test for Tet4-RK

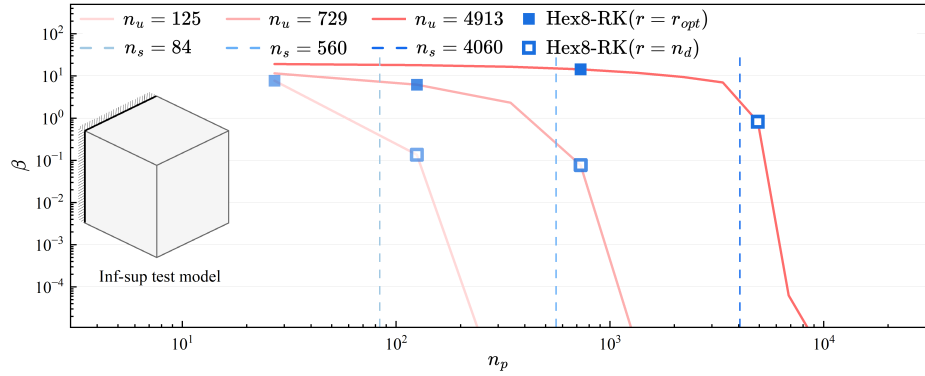


Figure 9: Inf-sup test for Hex8-RK

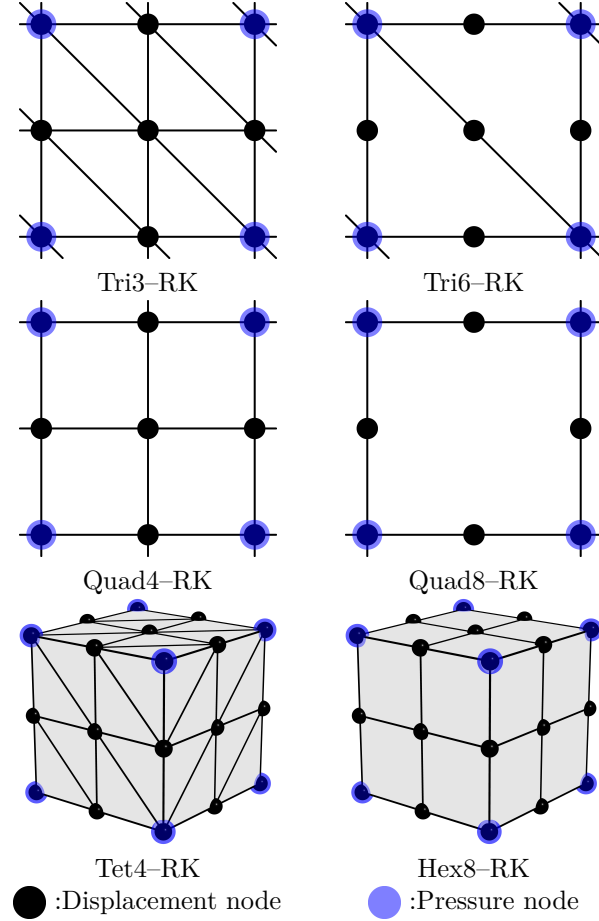


Figure 10: Nodal distribution schemes for mixed FE-meshfree formulations with  $r = r_{opt}$

393    **5. Numerical examples**

394    *5.1. Cantilever beam problem*

395    Consider the cantilever beam problem shown in Figure 11 with length  $L =$   
 396    48, width  $D = 12$ , and the incompressible material parameters are employed  
 397    with Young's modulus  $E = 3 \times 10^6$ , Poisson's ratio  $\nu = 0.5 - 10^{-8}$ . The left hand  
 398    side is fixed and the right side subject to a concentrated force  $P = 1000$ . All  
 399    the prescribed values in the boundary conditions are evaluated by the analytical  
 400    solution that is given as follows [61]:

$$\begin{cases} u_x(x) = -\frac{Py}{6EI} \left( (6L - 3x)x + (2 + \bar{\nu})(y^2 - \frac{D^2}{4}) \right) \\ u_y(x) = \frac{P}{6EI} \left( 3\bar{\nu}y^2(L - x) + (4 + 5\bar{\nu})\frac{D^2x}{4} + (3L - x)x^2 \right) \end{cases} \quad (60)$$

401    where  $I$  is the beam's moment of inertia,  $\bar{E}$  and  $\bar{\nu}$  are the material parameters  
 402    for plane strain hypothesis, they can be expressed by:

$$I = \frac{D^3}{12}, \quad \bar{E} = \frac{E}{1 - \nu^2}, \quad \bar{\nu} = \frac{\nu}{1 - \nu} \quad (61)$$

403    And correspondingly, the stress components are evaluated by

$$\begin{cases} \sigma_{xx} = -\frac{P(L - x)y}{I} \\ \sigma_{yy} = 0 \\ \sigma_{xy} = \frac{P}{2I} \left( \frac{D^2}{4} - y^2 \right) \end{cases} \quad (62)$$

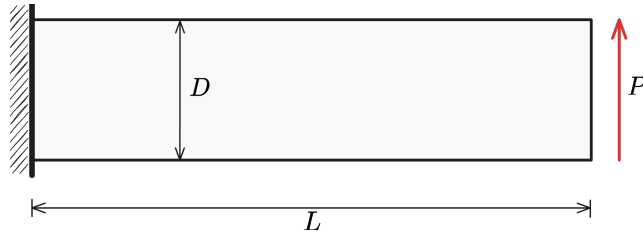


Figure 11: Illustration of cantilever beam problem

404    In this problem, the Quad4 element with  $16 \times 4$ ,  $32 \times 8$ ,  $64 \times 16$ ,  $128 \times$   
 405    32 grids, and Quad8 element with  $8 \times 2$ ,  $16 \times 4$ ,  $32 \times 8$ ,  $64 \times 16$  grids are  
 406    employed for displacement discretization. The pressure is discretized by linear  
 407    and quadratic meshfree approximations with 1.5 and 2.5 characterized support  
 408    sizes respectively. The strain and pressure errors with respect to pressure nodes  
 409     $n_p$  are displayed in Figure 12, where to avoid the interpolation error, the  
pressure nodes are uniformly distributed independent with displacement nodes

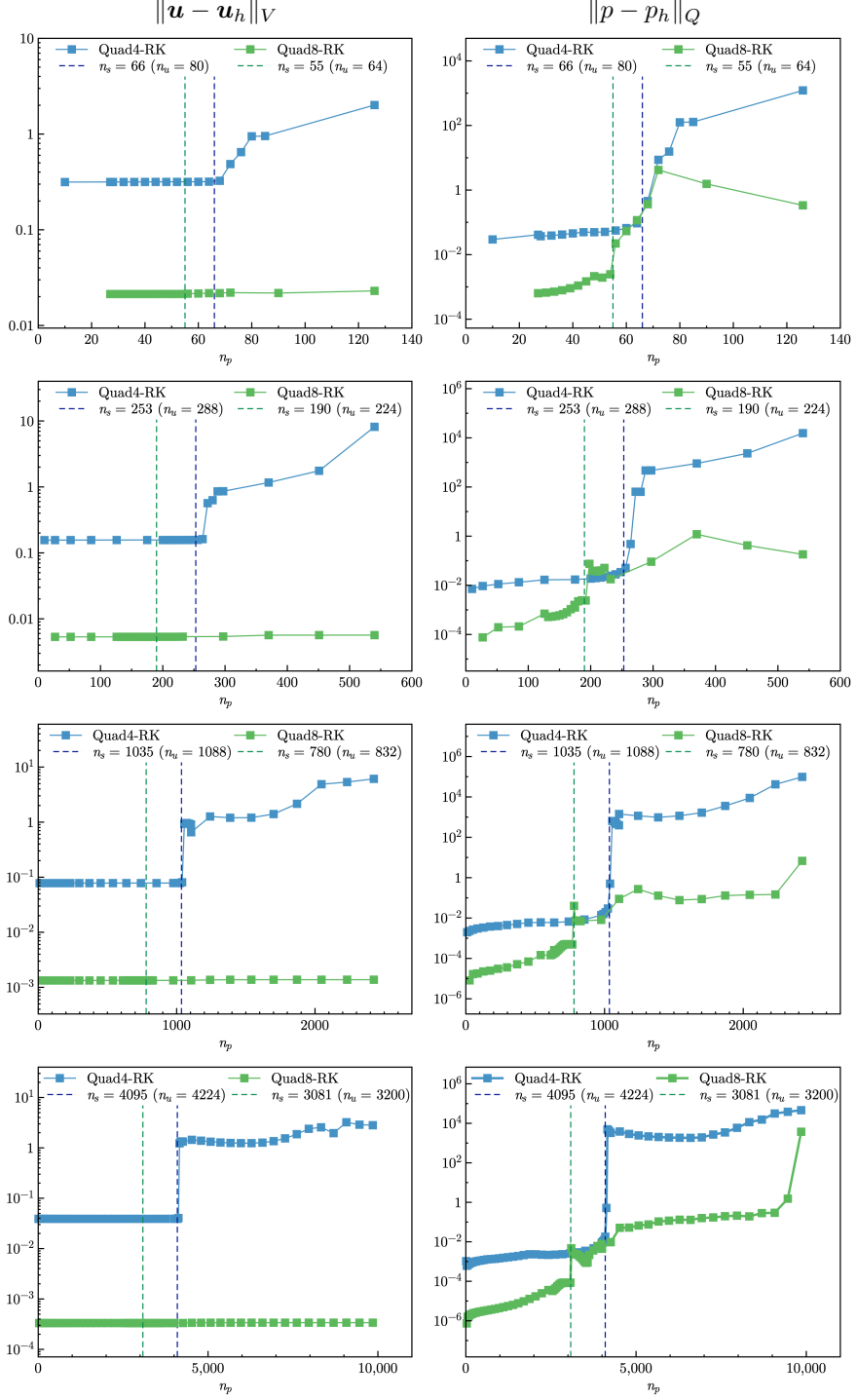


Figure 12: Strain and pressure errors vs.  $n_p$  for cantilever beam problem

by the same way in Section 4.2. The vertical dashed lines stand for the stabilized number  $n_s$ . The figure implies that the Quad8 shows better performance than Quad4, since the Quad8's strain results are stable no matter the constraint ratio is in the optimal range or not. And the Quad4's displacement errors increase as soon as  $n_p > n_s$ . However, both Quad4's and Quad8's pressure errors immediately increase while their constraint ratios are out of the optimal range, and Quad8 still has better results than Quad4. Figure 13 shows the strain and pressure error convergence comparisons with Quad4-RK, Quad8-RK with  $r = n_d$ ,  $r = r_{opt}$  and traditional 4-node quadrilateral displacement element with 1-node piecewise constant pressure (Q4P1), 8-node quadrilateral displacement element with 3-node piecewise linear pressure (Q8P3) for this cantilever beam problem, in which, except Quad8-RK( $r = n_d$ ) for strain error, all formulations with the traditional constraint ratio of  $r = n_d$  cannot ensure the optimal error convergence rates. The proposed mixed formulations with  $r = r_{opt}$  and Q4P1, Q8P3 can maintain the optimal error convergence ratio, except the strain error of Quad8-RK is a little larger than that of Q8P3, the proposed approaches show the best performance in accuracy.

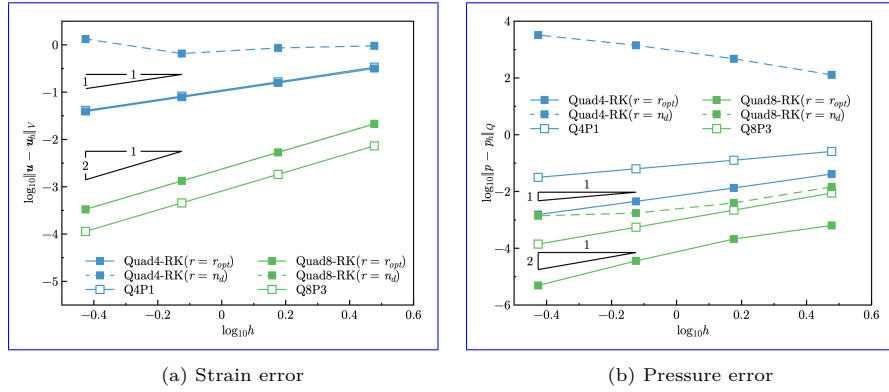


Figure 13: Error convergence study for cantilever beam problem

### 5.2. Plate with hole problem

429 Consider an infinite plate with a hole centered at the origin, as shown in  
 430 Figure 14, and at the infinity towards the  $x$ -direction subjected to a uniform  
 431 traction  $T = 1000$ . The geometric and material parameters for this problem are  
 432 that the ratio of the hole  $a = 1$ , Young's modulus  $E = 3 \times 10^6$ , and Poisson's  
 433 ratio  $\nu = 0.5 - 10^{-8}$ . The analytical solution of this problem refers to the  
 434 Michell solution [61] as:

$$\begin{cases} u_x(\rho, \theta) = \frac{Ta}{8\mu} \left( \frac{\rho}{a}(k+1) \cos \theta - \frac{2a^3}{\rho^3} \cos 3\theta + \frac{2a}{\rho} ((1+k) \cos \theta + \cos 3\theta) \right) \\ u_y(\rho, \theta) = \frac{Ta}{8\mu} \left( \frac{\rho}{a}(k-3) \sin \theta - \frac{2a^3}{\rho^3} \sin 3\theta + \frac{2a}{\rho} ((1-k) \sin \theta + \sin 3\theta) \right) \end{cases} \quad (63)$$

435 in which  $k = \frac{3-\nu}{1+\nu}$ ,  $\mu = \frac{E}{2(1+\nu)}$ . And the stress components are given by:

$$\begin{cases} \sigma_{xx} = T \left( 1 - \frac{a^2}{\rho^2} \left( \frac{3}{2} \cos 2\theta + \cos 4\theta \right) + \frac{3a^4}{2\rho^4} \cos 4\theta \right) \\ \sigma_{yy} = -T \left( \frac{a^2}{\rho^2} \left( \frac{1}{2} \cos 2\theta - \cos 4\theta \right) + \frac{3a^4}{2\rho^4} \cos 4\theta \right) \\ \sigma_{xy} = -T \left( \frac{a^2}{\rho^2} \left( \frac{1}{2} \sin 2\theta + \sin 4\theta \right) - \frac{3a^4}{2\rho^4} \sin 4\theta \right) \end{cases} \quad (64)$$

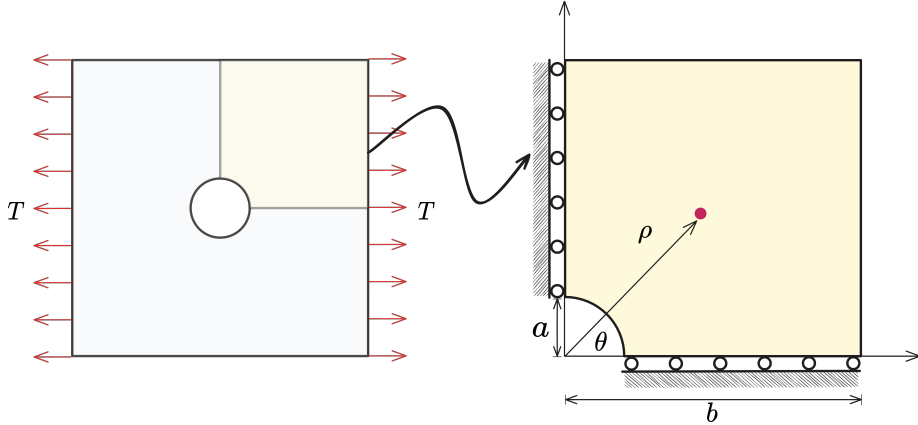


Figure 14: Illustration of plate with hole problem

436 According to the symmetry property of this problem, only a quarter model  
 437 with length  $b = 5$  is considered as shown in Figure 14. The displacement is  
 438 discretized by 3-node and 6-node triangular elements with 81, 299, 1089, and  
 439 4225 nodes. The corresponding linear and quadratic meshfree formulations are  
 440 employed for pressure discretization, and the characterized support sizes are  
 441 chosen as 1.5 and 2.5, respectively. Figure 15 studies the relationship between  
 442 strain, pressure errors, and  $n_p$  using the nodal distributions uniformly related  
 443 to displacement nodes. Unlike the quadrilateral element case in Section 5.1,  
 444 the quadratic Tri6-RK shows worse results while the constraint ratio is out of  
 445 the optimal range. And Tri3-RK exhibits less sensitivity in strain error than  
 446 Tri6-RK, but its error is increasing while  $n_p$  goes up. Both Tri3-RK and Tri6-  
 447 RK with constraint ratios under the optimal range perform acceptably. The  
 448 corresponding error convergence study is presented in Figure 16, the traditional  
 449 MINI element and the 6-node triangular displacement element with 3-node  
 450 continuous triangular pressure element (T6C3) are employed for comparison.  
 451 The results show that only Tri3-RK with  $r = 2$  shows a comparable result with  
 452 the optimal one with  $r = r_{opt}$ . The other formulations with the traditional  
 453 constraint ratio show lower accuracy and error convergence rates.

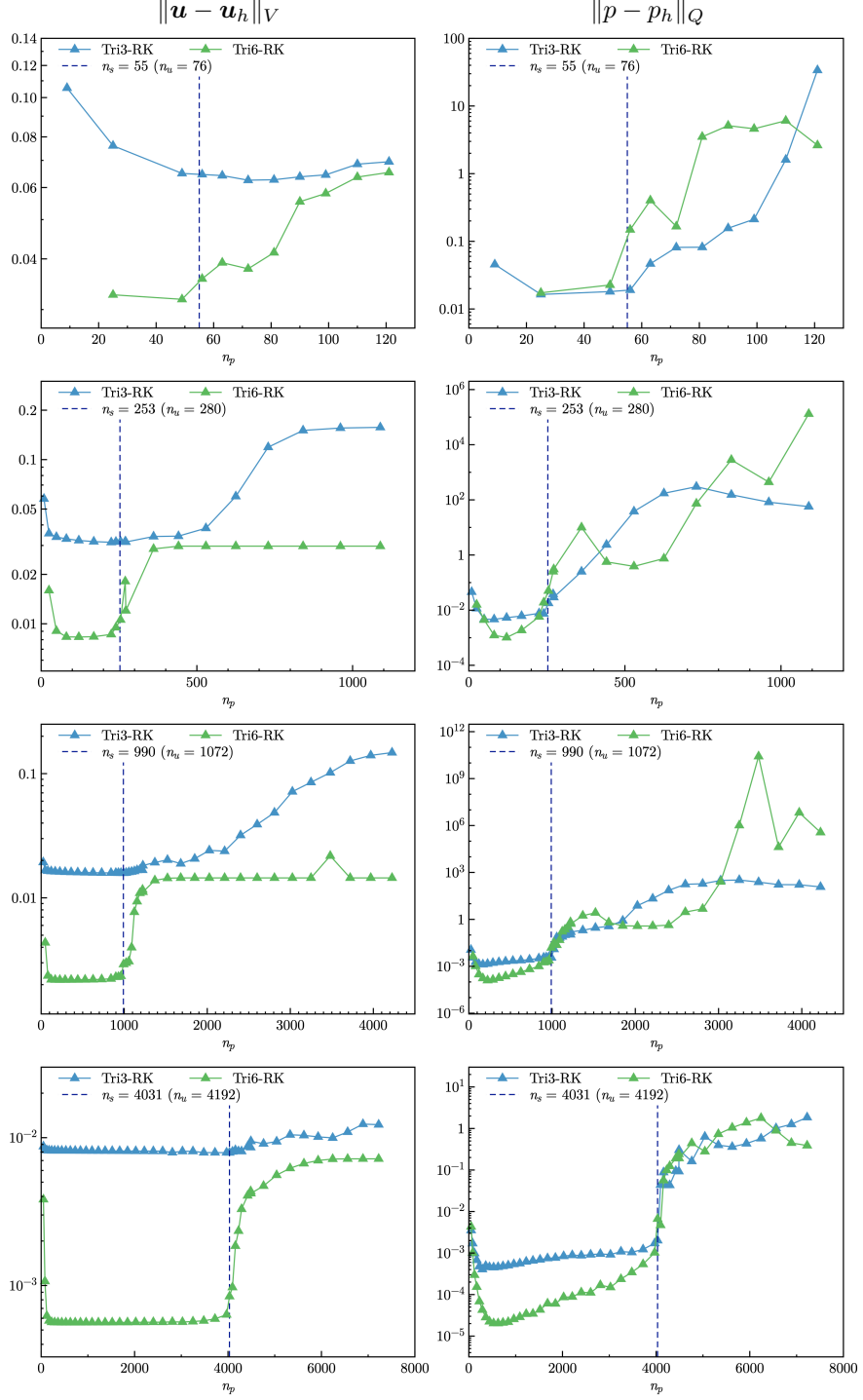


Figure 15: Strain and pressure errors vs.  $n_p$  for plate with hole problem

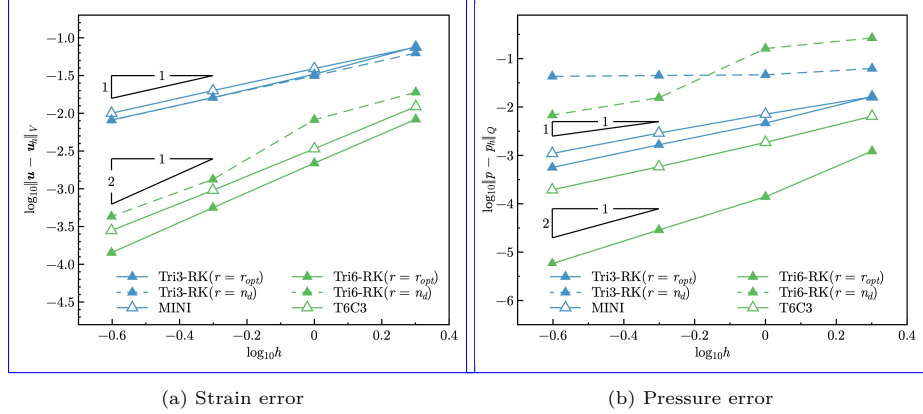


Figure 16: Error convergence study for plate with a hole problem

### 454 5.3. Cook's membrane problem

455 The Cook's membrane problem [12] is used herein for stability analysis of  
 456 pressure. The geometry of this problem is shown in Figure 17, in which the left  
 457 hand side is fixed and the right hand side subjects a concentrated force  $P = 6.25$   
 458 in the  $y$ -direction. The material parameters are Young's modulus  $E = 70.0$  and  
 459 Poisson's ratio  $\nu = 0.5 - 10^{-8}$ .

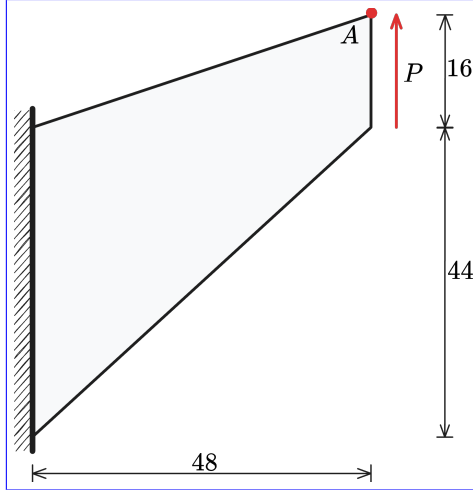


Figure 17: Illustration of Cook's membrane problem

460 In this test, we evaluated the convergence properties by comparing the  
 461 vertical displacement at point  $A$  against a reference value of 28.0. As shown in  
 462 Figure 18 illustrates, the methods employing  $r = r_{opt}$  produced results that were  
 463 notably closer to this reference value than those using  $r = n_d$ . Furthermore, to

464 investigate stability. Figures 19–22 show the pressure contour plots for non-  
 465 uniform Tri3–RK, Tri6–RK, Quad4–RK, and Quad8–RK formulations with  
 466  $r = n_d$  and  $r = r_{opt}$ , respectively. The reproducing kernel meshfree approximations  
 467 are employed for pressure discretization with characterized support  
 468 sizes of 1.5 for the linear basis function and 2.5 for the quadratic basis function.  
 469 The results imply that the pressure contour plots with the optimal constraint  
 470 ratio  $r = r_{opt}$  show a more stable and smooth pressure distribution compared  
 471 to those with the traditional constraint ratio  $r = n_d$ .

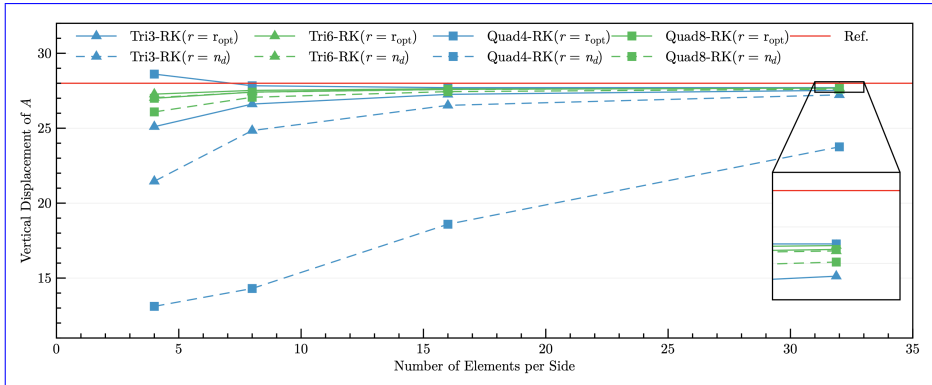


Figure 18: Convergence comparison of the vertical displacement at point A for Cook's membrane problem

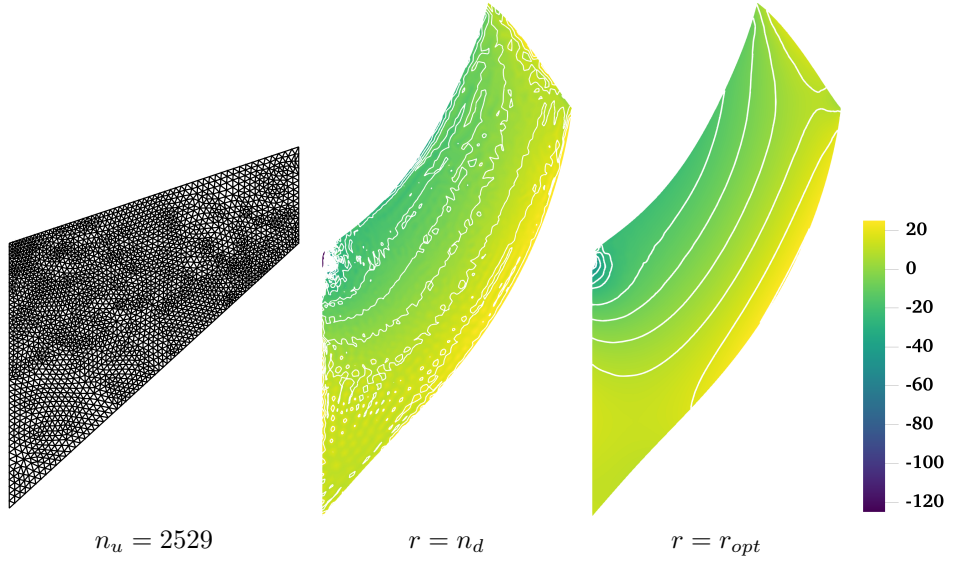


Figure 19: Pressure contour plots for Cook's membrane problem using Tri3–RK

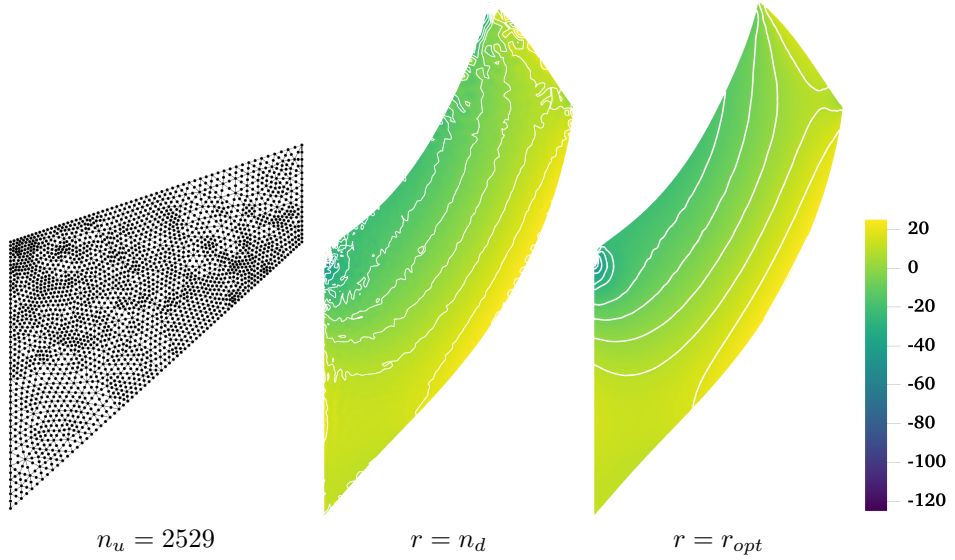


Figure 20: Comparison of pressure contour plots for Cook's membrane problem using Tri6–RK

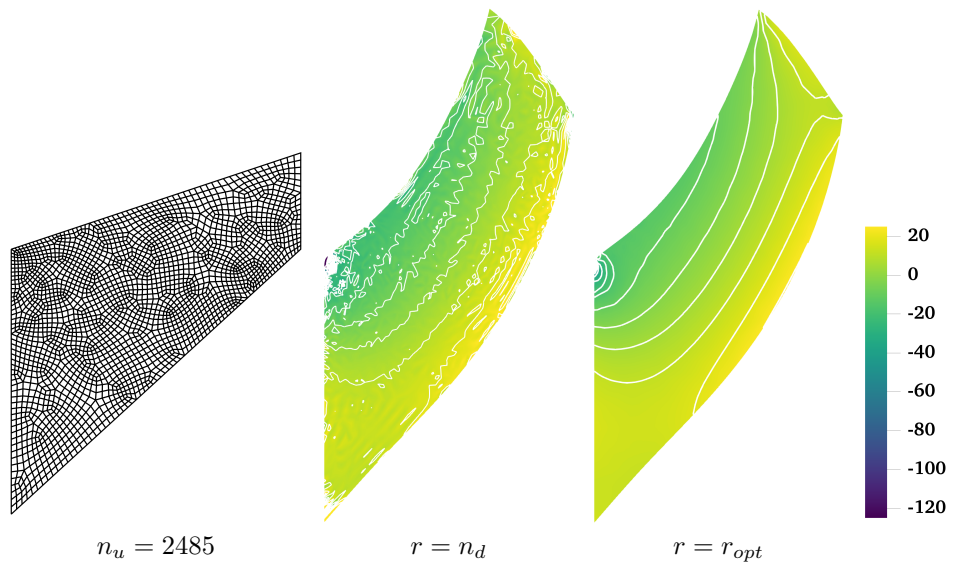


Figure 21: Comparison of pressure contour plots for Cook's membrane problem using Quad4–RK

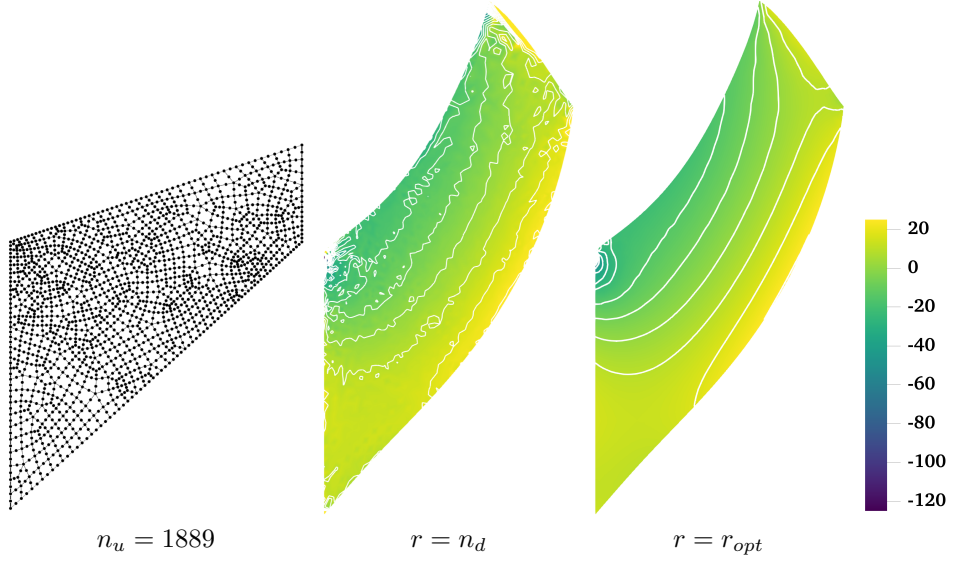


Figure 22: Comparison of pressure contour plots for Cook's membrane problem using Quad8-RK

472     5.4. *Block under compression problem*

473     The incompressible block problem [62] shown in Figure 23 is considered for  
 474     testing 3D mixed formulations. The block's dimensions are  $2L \times 2L \times L$ ,  $L = 1$ .  
 475     At the center of the top surface of the block is applied a pressure load  $P$  with  
 476     the area of  $L \times L$ . Due to the symmetry of this problem, only a quarter model is  
 477     considered. The Young's modulus and Poisson's ratio are set as  $E = 240.56839$   
 478     and  $\nu = 0.5 - 10^{-8}$ , respectively.

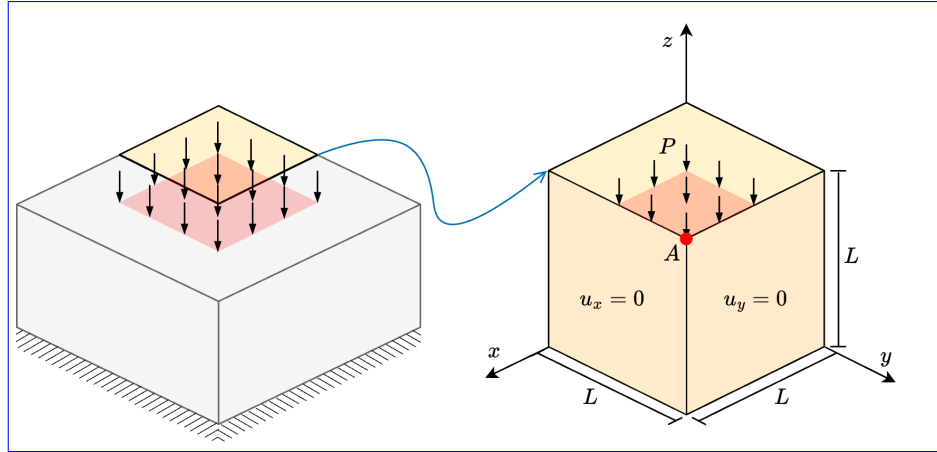


Figure 23: Illustration of block under compression problem

479 The convergence properties of the mixed formulations are evaluated by  
 480 comparing the compression level at point A under various loading conditions  
 481  $P/P_0$ , where  $P_0 = 4$ . As shown in Figure 24, all the results exhibit good  
 482 convergence behavior across different loading levels. Figures 25, 26 study the  
 483 pressure stability of 3D mixed FE-meshfree formulations, Tet4-RK and Hex8-  
 484 RK, with non-uniform nodal distribution, while the pressure is discretized by  
 485 linear meshfree approximations with a characterized support size of 1.5. The  
 486 corresponding results also show the well performance of the proposed optimal  
 487 constraint ratio  $r = r_{opt}$ . The mixed formulations with the traditional constraint  
 488 ratio  $r = n_d$  show comparable displacement results, but exhibit significant pres-  
 489 sure instability.

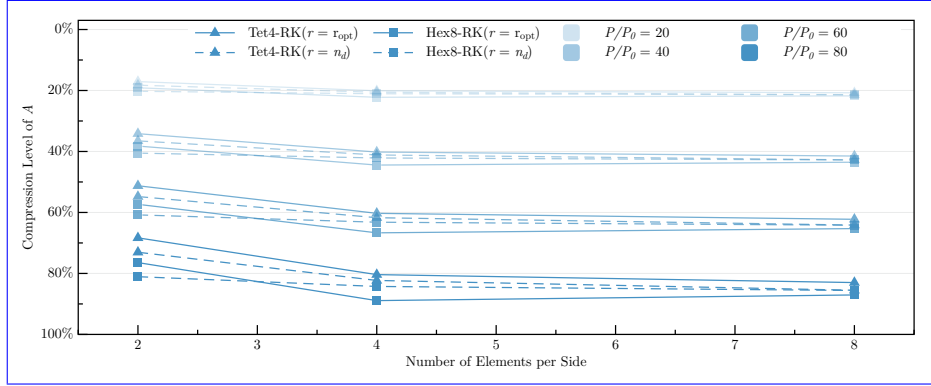


Figure 24: Convergence comparison of compression level (%) at point A for block under compression problem

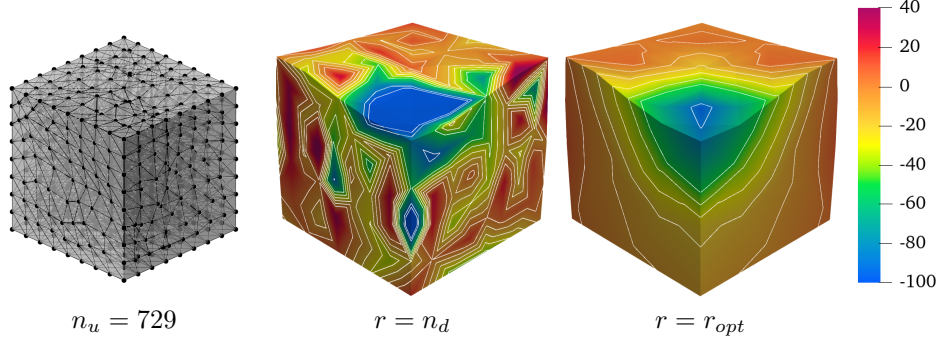


Figure 25: Comparison of pressure contour plots for block under compression problem using Tet4-RK

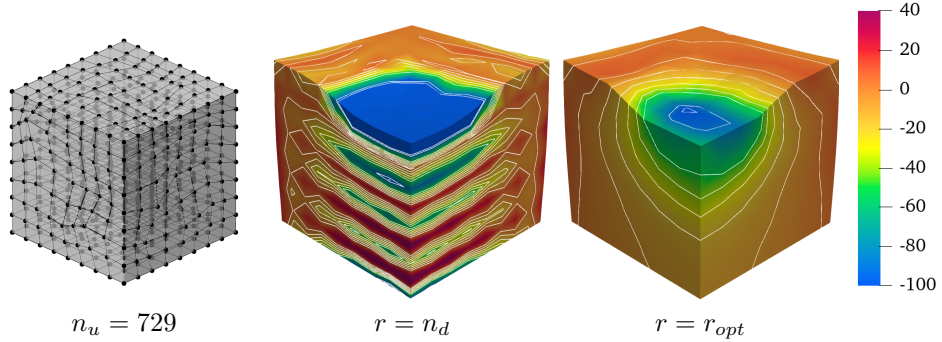


Figure 26: Comparison of pressure contour plots for block under compression problem using Hex8–RK

## 490 6. Conclusion

491 This paper proposes a novel optimal constraint ratio derived from the inf–sup  
 492 condition to address volumetric locking. The optimal constraint ratio requires  
 493 that, for a given number of displacement DOFs, the number of pressure DOFs  
 494 should remain below a stabilized number determined by the proposed inf–sup  
 495 value estimator. For a well-posed nodal distribution, simply counting the dis-  
 496 placement and pressure DOFs can determine whether the formulation satisfies  
 497 the inf–sup condition. Compared to the traditional constraint ratio, the pro-  
 498 posed ratio is theoretically grounded in the inf–sup condition and thus is more  
 499 precise.

500 To implement this constraint ratio, a mixed finite element (FE) and meshfree  
 501 formulation is developed. Displacements are discretized using 3-node and 6-node  
 502 triangular elements, 4-node and 8-node quadrilateral elements in 2D, and 4-node  
 503 tetrahedral and 8-node hexahedral elements in 3D. Correspondingly, linear and  
 504 quadratic reproducing kernel meshfree approximations are used for pressure  
 505 discretization. The reproducing kernel approximation equips globally smooth  
 506 shape functions, allowing arbitrary pressure DOF placement without the limit  
 507 of element.

508 Inf–sup tests for mixed FE–meshfree formulations with different constraint  
 509 ratios verify the effectiveness of the proposed inf–sup value estimator. For effi-  
 510 ciency and ease of implementation, the final nodal distribution scheme selects  
 511 every other displacement node as a pressure node, ensuring the optimal con-  
 512 straint ratio and satisfying the inf–sup condition.

513 A series of 2D and 3D incompressible elasticity examples demonstrate the  
 514 effectiveness of the proposed mixed formulation. Results show that formulations  
 515 with the optimal constraint ratio yield accurate displacement and pressure solu-  
 516 tions. When the constraint ratio exceeds the optimal value, errors rise sharply  
 517 to unacceptable levels, with the 8-node quadrilateral element being the only  
 518 exception that maintains good displacement accuracy. Error convergence stud-  
 519 ies and pressure contour plots further confirm that mixed formulations with

520 the optimal constraint ratio achieve optimal convergence rates and effectively  
521 suppress pressure oscillations.

522 **Acknowledgment**

523 The support of this work by the National Natural Science Foundation of  
524 China (12102138), the Natural Science Foundation of Fujian Province of China  
525 (2023J01108) and the Fundamental Research Funds of Central Universities  
526 (ZQN-1014) is gratefully acknowledged.

527 **References**

- 528 [1] F. Brezzi, M. Fortin, Mixed and Hybrid Finite Element Methods, Vol. 15 of  
529 Springer Series in Computational Mathematics, Springer, New York, NY,  
530 1991.
- 531 [2] T. J. Hughes, The Finite Element Method: Linear Static and Dynamic  
532 Finite Element Analysis, Prentice Hall, New Jersey, 2000.
- 533 [3] I. Babuška, R. Narasimhan, The Babuška-Brezzi condition and the patch  
534 test: An example, Computer Methods in Applied Mechanics and Engineering 140 (1-2) (1997) 183–199.
- 535 [4] K. J. Bathe, Finite Element Procedures, Prentice Hall, Englewood Cliffs,  
536 New Jersey, 1996.
- 537 [5] D. S. Malkus, Eigenproblems associated with the discrete LBB condition for  
538 incompressible finite elements, International Journal of Engineering Science 19 (10) (1981) 1299–1310.
- 539 [6] D. Chapelle, K. J. Bathe, The inf-sup test, Computers & Structures 47 (4)  
540 (1993) 537–545.
- 541 [7] F. Brezzi, K. J. Bathe, Studies of finite element procedures the inf-sup  
542 condition equivalent forms and applications.
- 543 [8] D. Gallistl, Rayleigh-Ritz approximation of the inf-sup constant for the  
544 divergence, Mathematics of Computation 88 (315) (2019) 73–89.
- 545 [9] P. Hood, C. Taylor, Navier-Stokes equations using mixed interpolation,  
546 Finite element methods in flow problems (1974) 121–132.
- 547 [10] D. S. Malkus, T. J. Hughes, Mixed finite element methods - Reduced and  
548 selective integration techniques: A unification of concepts, Computer Meth-  
549 ods in Applied Mechanics and Engineering 15 (1) (1978) 63–81.
- 550 [11] T. Shilt, R. Deshmukh, J. J. McNamara, P. J. O’Hara, Solution of nearly  
551 incompressible field problems using a generalized finite element approach,  
552 Computer Methods in Applied Mechanics and Engineering 368 (2020)  
553 113165.

- 556 [12] J. C. Simo, M. S. Rifai, A class of mixed assumed strain methods and  
 557 the method of incompatible modes, International Journal for Numerical  
 558 Methods in Engineering 29 (8) (1990) 1595–1638.
- 559 [13] M. Broccardo, M. Micheloni, P. Krysl, Assumed-deformation gradient finite  
 560 elements with nodal integration for nearly incompressible large deformation  
 561 analysis, International Journal for Numerical Methods in Engineering 78 (9)  
 562 (2009) 1113–1134.
- 563 [14] W. M. Coombs, T. J. Charlton, M. Cortis, C. E. Augarde, Overcoming vol-  
 564 umetric locking in material point methods, Computer Methods in Applied  
 565 Mechanics and Engineering 333 (2018) 1–21.
- 566 [15] S. Saloustros, M. Cervera, S. Kim, M. Chiumenti, Accurate and locking-free  
 567 analysis of beams, plates and shells using solid elements, Computational  
 568 Mechanics 67 (2021) 883–914.
- 569 [16] J. Simo, R. Taylor, K. Pister, Variational and projection methods for the  
 570 volume constraint in finite deformation elasto-plasticity, Computer Meth-  
 571 ods in Applied Mechanics and Engineering 51 (1-3) (1985) 177–208.
- 572 [17] C. R. Dohrmann, P. B. Bochev, A stabilized finite element method for the  
 573 Stokes problem based on polynomial pressure projections, International  
 574 Journal for Numerical Methods in Fluids 46 (2) (2004) 183–201.
- 575 [18] A. Valverde-González, J. Reinoso, B. Dortdivanlioglu, M. Paggi, Locking  
 576 treatment of penalty-based gradient-enhanced damage formulation for fail-  
 577 ure of compressible and nearly incompressible hyperelastic materials, Com-  
 578 putational Mechanics 72 (2023) 635–662.
- 579 [19] B.-B. Xu, F. Peng, P. Wriggers, Stabilization-free virtual element method  
 580 for finite strain applications, Computer Methods in Applied Mechanics and  
 581 Engineering 417 (2023) 116555.
- 582 [20] F. S. Liguori, A. Madeo, S. Marfia, G. Garcea, E. Sacco, A stabilization-  
 583 free hybrid virtual element formulation for the accurate analysis of 2D  
 584 elasto-plastic problems, Computer Methods in Applied Mechanics and En-  
 585 gineering 431 (2024) 117281.
- 586 [21] R. Alves de Sousa, R. Natal Jorge, R. Fontes Valente, J. César de Sá, A new  
 587 volumetric and shear locking-free 3D enhanced strain element, Engineering  
 588 Computations 20 (7) (2003) 896–925.
- 589 [22] K.-J. Bathe, The inf-sup condition and its evaluation for mixed finite ele-  
 590 ment methods, Computers & Structures 79 (2) (2001) 243–252.
- 591 [23] T. J. R. Hughes, Multiscale phenomena: Green's functions, the Dirichlet-  
 592 to-Neumann formulation, subgrid scale models, bubbles and the origins of  
 593 stabilized methods, Computer Methods in Applied Mechanics and Engi-  
 594 neering 127 (1) (1995) 387–401.

- 595 [24] R. Rossi, R. Zorrilla, R. Codina, A stabilised displacement-volumetric  
 596 strain formulation for nearly incompressible and anisotropic materials,  
 597 Computer Methods in Applied Mechanics and Engineering 377 (2021)  
 598 113701.
- 599 [25] E. Karabelas, M. A. F. Gsell, G. Haase, G. Plank, C. M. Augustin, An  
 600 accurate, robust, and efficient finite element framework with applications to  
 601 anisotropic, nearly and fully incompressible elasticity, Computer Methods  
 602 in Applied Mechanics and Engineering 394 (2022) 114887.
- 603 [26] R. Codina, I. Castañar, J. Baiges, Finite element approximation of stabi-  
 604 lized mixed models in finite strain hyperelasticity involving displacements  
 605 and stresses and/or pressure—An overview of alternatives, International  
 606 Journal for Numerical Methods in Engineering (2024) e7540.
- 607 [27] L. Moreno, R. Wuechner, A. Larese, A mixed stabilized MPM formula-  
 608 tion for incompressible hyperelastic materials using Variational Subgrid-  
 609 Scales, Computer Methods in Applied Mechanics and Engineering 435  
 610 (2025) 117621.
- 611 [28] T. J. R. Hughes, L. P. Franca, M. Balestra, A new finite element formu-  
 612 lation for computational fluid dynamics: V. Circumventing the babuška-  
 613 brezzi condition: A stable Petrov-Galerkin formulation of the stokes prob-  
 614 lem accommodating equal-order interpolations, Computer Methods in Ap-  
 615 plied Mechanics and Engineering 59 (1) (1986) 85–99.
- 616 [29] A. N. Brooks, T. J. R. Hughes, Streamline upwind/Petrov-Galerkin formu-  
 617 lations for convection dominated flows with particular emphasis on the in-  
 618 compressible Navier-Stokes equations, Computer Methods in Applied Me-  
 619 chanics and Engineering 32 (1) (1982) 199–259.
- 620 [30] L. He, L. Jing, M. Feng, New stabilized mixed finite element methods for  
 621 two-field poroelasticity with low permeability, Applied Mathematics and  
 622 Computation 494 (2025) 129285.
- 623 [31] D. N. Arnold, F. Brezzi, M. Fortin, A stable finite element for the Stokes  
 624 equations, CALCOLO 21 (4) (1984) 337–344.
- 625 [32] F. Auricchio, L. Beirão da Veiga, C. Lovadina, A. Reali, A stability study of  
 626 some mixed finite elements for large deformation elasticity problems, Com-  
 627 puter Methods in Applied Mechanics and Engineering 194 (9-11) (2005)  
 628 1075–1092.
- 629 [33] A. Quarteroni, A. Valli, Numerical Approximation of Partial Differen-  
 630 tial Equations, Springer Series in Computational Mathematics, Springer,  
 631 Berlin, 1994.
- 632 [34] M. Crouzeix, P. Raviart, Conforming and nonconforming finite ele-  
 633 ment methods for solving the stationary Stokes equations I, Revue

- 634        fran aise d'automatique informatique recherche op rationnelle. Math m   
 635        atique 7 (R3) (1973) 33 75.
- 636        [35] U. Brink, E. Stein, On some mixed finite element methods for incompressible and nearly incompressible finite elasticity, Computational Mechanics  
 637        19 (1) (1996) 105 119.
- 639        [36] T. Belytschko, Y. Y. Lu, L. Gu, Element-free Galerkin methods, International Journal for Numerical Methods in Engineering 37 (2) (1994) 229 256.
- 641        [37] W. K. Liu, S. Jun, Y. F. Zhang, Reproducing kernel particle methods, International Journal for Numerical Methods in Fluids 20 (8-9) (1995) 1081 1106.
- 644        [38] C. Rodriguez, T.-H. Huang, A variationally consistent reproducing kernel enhanced material point method and its applications to incompressible materials, Computational Mechanics (2023) 1 20.
- 647        [39] S. W. Chi, J. S. Chen, H. Y. Hu, A weighted collocation on the strong form with mixed radial basis approximations for incompressible linear elasticity, Computational Mechanics 53 (2) (2014) 309 324.
- 650        [40] L. Wang, Z. Qian, Y. Zhou, Y. Peng, A weighted meshfree collocation method for incompressible flows using radial basis functions, Journal of Computational Physics 401 (2020) 108964.
- 653        [41] A. Ortiz-Bernardin, M. Puso, N. Sukumar, Improved robustness for nearly-incompressible large deformation meshfree simulations on Delaunay tessellations, Computer Methods in Applied Mechanics and Engineering 293 (2015) 348 374.
- 657        [42] T. J. Hughes, J. A. Cottrell, Y. Bazilevs, Isogeometric analysis: CAD, finite elements, NURBS, exact geometry and mesh refinement, Computer Methods in Applied Mechanics and Engineering 194 (39-41) (2005) 4135 4195.
- 661        [43] F. Auricchio, L. Beir o da Veiga, C. Lovadina, A. Reali, The importance of the exact satisfaction of the incompressibility constraint in nonlinear elasticity: Mixed FEMs versus NURBS-based approximations, Computer Methods in Applied Mechanics and Engineering 199 (5) (2010) 314 323.
- 665        [44] A. Huerta, S. Fern andez-M ndez, Locking in the incompressible limit for the element-free Galerkin method, International Journal for Numerical Methods in Engineering 51 (11) (2001) 1361 1383.
- 668        [45] J. Dolbow, T. Belytschko, Volumetric locking in the element free Galerkin method, International Journal for Numerical Methods in Engineering 46 (6) (1999) 925 942.

- 671 [46] G. Moutsanidis, J. J. Koester, M. R. Tupek, J.-S. Chen, Y. Bazilevs, Treatment  
 672 of near-incompressibility in meshfree and immersed-particle methods,  
 673 Computational Particle Mechanics 7 (2) (2020) 309–327.
- 674 [47] G. Moutsanidis, W. Li, Y. Bazilevs, Reduced quadrature for FEM, IGA  
 675 and meshfree methods, Computer Methods in Applied Mechanics and En-  
 676 gineering 373 (2021) 113521.
- 677 [48] Z.-Y. Wang, Y.-F. Jin, Z.-Y. Yin, Y.-Z. Wang, Overcoming volumetric  
 678 locking in stable node-based smoothed particle finite element method with  
 679 cubic bubble function and selective integration, International Journal for  
 680 Numerical Methods in Engineering 123 (24) (2022) 6148–6169.
- 681 [49] T. Elguedj, Y. Bazilevs, V. Calo, T. Hughes,  $B^-$  and  $F^-$  projection meth-  
 682 ods for nearly incompressible linear and non-linear elasticity and plasticity  
 683 using higher-order NURBS elements, Computer Methods in Applied Me-  
 684 chanics and Engineering 197 (33-40) (2008) 2732–2762.
- 685 [50] J. S. Chen, S. Yoon, H. P. Wang, W. K. Liu, An improved reproducing  
 686 kernel particle method for nearly incompressible finite elasticity, Computer  
 687 Methods in Applied Mechanics and Engineering 181 (1) (2000) 117–145.
- 688 [51] C. M. Goh, P. M. F. Nielsen, M. P. Nash, A stabilised mixed mesh-  
 689 free method for incompressible media: Application to linear elasticity and  
 690 Stokes flow, Computer Methods in Applied Mechanics and Engineering 329  
 691 (2018) 575–598.
- 692 [52] D. S. Bombarde, M. Agrawal, S. S. Gautam, A. Nandy, Hellinger–Reissner  
 693 principle based stress–displacement formulation for three-dimensional iso-  
 694 geometric analysis in linear elasticity, Computer Methods in Applied Me-  
 695 chanics and Engineering 394 (2022) 114920.
- 696 [53] H. Casquero, M. Golestanian, Vanquishing volumetric locking in quadratic  
 697 NURBS-based discretizations of nearly-incompressible linear elasticity:  
 698 CAS elements, Computational Mechanics 73 (6) (2024) 1241–1252.
- 699 [54] A. Huerta, Y. Vidal, P. Villon, Pseudo-divergence-free element free  
 700 Galerkin method for incompressible fluid flow, Computer Methods in Ap-  
 701 plied Mechanics and Engineering 193 (12-14) (2004) 1119–1136.
- 702 [55] C. T. Wu, W. Hu, J. S. Chen, A meshfree-enriched finite element method  
 703 for compressible and near-incompressible elasticity, International Journal  
 704 for Numerical Methods in Engineering 90 (7) (2012) 882–914.
- 705 [56] T. Vu-Huu, C. Le-Thanh, H. Nguyen-Xuan, M. Abdel-Wahab, A high-  
 706 order mixed polygonal finite element for incompressible Stokes flow analy-  
 707 sis, Computer Methods in Applied Mechanics and Engineering 356 (2019)  
 708 175–198.

- 709 [57] E. Stein, R. de Borst, T. J. R. Hughes (Eds.), Encyclopedia of Computational Mechanics, John Wiley, Chichester, West Sussex, 2004.
- 710
- 711 [58] I. Babuška, J. Osborn, Eigenvalue Problems, in: Handbook of Numerical Analysis, Vol. 2 of Finite Element Methods (Part 1), Elsevier, 1991, pp. 641–787.
- 712
- 713
- 714 [59] K. Yosida, Functional Analysis, 6th Edition, Classics in Mathematics, Springer-Verlag, Berlin Heidelberg, 1995.
- 715
- 716 [60] [J. Wu, D. Wang, An accuracy analysis of Galerkin meshfree methods accounting for numerical integration, Computer Methods in Applied Mechanics and Engineering 375 \(2021\) 113631.](#)
- 717
- 718
- 719 [61] S. Timoshenko, J. Goodier, Theory of Elasticity, Engineering Mechanics Series, McGraw-Hill, 1969.
- 720
- 721 [62] [S. Reese, P. Wriggers, B. D. Reddy, A new locking-free brick element technique for large deformation problems in elasticity, Computers & Structures 75 \(3\) \(2000\) 291–304.](#)
- 722
- 723